The Astronomical Journal, 123:1528–1547, 2002 March

CIRCUMSTELLAR DISK CANDIDATES IDENTIFIED IN NGC 2264

L. M. Rebull,[1] R. B. Makidon,[2] S. E. Strom,[3] L. A. Hillenbrand,[4] A. Birmingham,[5]
Brian M. Patten,[6] B. F. Jones,[7] H. Yagi,[8] and Mark T. Adams[9]

Received 2001 October 2; accepted 2001 November 28

ABSTRACT

We present an optical and near-infrared study of a $45' \times 45'$ field in NGC 2264, which includes both S Mon and the Cone Nebula. We report photometry at optical ($UBVR_CI_C$) and near-infrared (JHK) wavelengths for ~5600 stars and spectroscopic classifications for ~400 of these stars. We identify circumstellar disk candidates using three techniques: excess ultraviolet ($U-V$) emission, excess near-IR ($I-K$ and $H-K$) emission, and Hα emission-line equivalent widths for those stars with spectra. We find generally good correlation between disk indicators thought to originate from different physical processes. We find little if any evolution of disk fraction with stellar age or mass. However, when we derive mass accretion rates ($\dot{M}$) from the excess emission at U, we find that $\dot{M}$ decreases with age over the age range spanned by our data, ~0.1–5 Myr, and increases with mass over the range ~0.25–1 $M_\odot$. These findings are comparable to results found previously by us in the Orion Nebula cluster flanking fields.

Key words: open clusters and associations: individual (NGC 2264) — stars: pre–main-sequence

On-line material: machine-readable tables

1. INTRODUCTION

Over the past 15 years considerable effort has been invested in establishing the frequency with which circumstellar accretion disks surround pre–main-sequence (PMS) stars as a function of age (e.g., Strom et al. 1989; Hollenbach, Yorke, & Johnstone 2000; Sargent & Beckwith 1994). With few exceptions, these studies make use of near-infrared (typically K-band) excesses to establish disk frequencies.

More recent studies have focussed on using complementary disk indicators, such as $U-V$ excess and selected strong emission lines, to diagnose not only the presence of accretion disks but to quantify disk accretion rates for PMS stars spanning a range of masses and ages (Gullbring et al. 1998; Hartmann et al. 1998; Rebull et al. 2000, hereafter R00; Calvet, Hartmann, & Strom 2000, and references therein). Although sample sizes are still modest and results therefore preliminary, it appears that among solar-type stars, typical disk accretion rates at ages ~1 Myr are $\sim 10^{-8}\ M_\odot\ \mathrm{yr}^{-1}$ and decrease as the stars evolve, with the range of disk accretion rates encompassing higher values among higher mass stars—reaching $\sim 10^{-6.5}$–$10^{-7}\ M_\odot\ \mathrm{yr}^{-1}$ for stars of ~1 $M_\odot$, but only $\sim 10^{-8}$–$10^{-9}\ M_\odot\ \mathrm{yr}^{-1}$ for stars of ~0.3 $M_\odot$ (R00).

We present here a study of the pre–main-sequence population in the young cluster NGC 2264, which is part of the Mon OB1 association. Our goals are (1) to identify disk candidates among the cluster members using multiple disk indicators, (2) to quantify accretion properties, and (3) to compare with previous results obtained using similar techniques in the Orion Nebula cluster flanking fields region.

PMS stars have been identified previously in NGC 2264 using a variety of methods, including early Hα photographic spectroscopy (Herbig 1954), Hα objective prism spectroscopy (Ogura 1984), Hα narrowband photometry (e.g., Sung, Bessell, & Lee 1997; Park et al. 2000), irregular variability (e.g., Adams, Strom, & Strom 1983), JHK photometry (e.g., Lada, Young, & Greene 1993), and *ROSAT* x-ray flux (Flaccomio et al. 2000; Patten et al. 1994; Simon, Cash, & Snow 1985). NGC 2264, at ~3 Myr (Park et al. 2000), is slightly older than Orion (~1–3 Myr, R00; Hillenbrand 1997), and is further away (760 pc, Sung et al. 1997; Park et al. 2000 vs. 470 pc, Genzel et al. 1981; Walker 1969), though still close enough to allow examination of the initial mass function (IMF) down to very low masses. Sung et al. (1997) found that the shape of the IMF in NGC 2264 is very similar to that of Orion, despite the much lower surface density of stars in NGC 2264. This lower surface density in theory could present a problem in that the cluster is only ~2° out of the Galactic plane, and thus the potential for field star contamination is high; however, a molecular cloud fortunately located behind the cluster aids in blocking out background stars. Wolf-Chase, Walker, & Lada (1995) found a total cloud mass of ~1900–2500 $M_\odot$.

This study is based on $UBVR_CI_C$ and JHK imaging surveys of a $45' \times 45'$ field in NGC 2264 containing ~5600 stars, along with spectroscopy of ~400 candidate members.

[1] National Research Council Resident Research Associate, NASA/Jet Propulsion Laboratory, Mail Stop 169-506, 4800 Oak Grove Drive, Pasadena, CA 91109; luisa.rebull@jpl.nasa.gov.
[2] Space Telescope Science Institute, 3700 San Martin Drive, Baltimore, MD 21218.
[3] National Optical Astronomical Observatory, 950 North Cherry Avenue, Tucson, AZ 87526.
[4] Department of Astronomy, California Institute of Technology, Pasadena, CA 91125.
[5] Five College Astronomy Department, Amherst College, Amherst, MA 01002.
[6] Harvard-Smithsonian Center for Astrophysics, 60 Garden Street, Cambridge, MA 02138.
[7] UCO/Lick Observatory, University of California, Santa Cruz, Santa Cruz, CA 95064.
[8] Five College Department of Astronomy, University of Massachusetts, Graduate Research Tower, Amherst, MA 01003.
[9] University of Texas/McDonald Observatory, P.O. Box 1337, Fort Davis, TX 79734-1337.

These data allow us to (1) locate candidate members in a color-magnitude diagram and derive masses and ages; (2) select stars apparently surrounded by disks using $U-V$, $I-K$, and $H-K$ excesses and Hα emission as disk indicators; (3) deduce the frequency of disks as a function of stellar age and mass; (4) derive accretion rates from U-band excesses for stars with $M \lesssim 1\ M_{\odot}$ and compare these results with those for Orion (R00) and Taurus-Auriga (Hartmann et al. 1998); and (5) derive the stellar mass and age dependence of $\dot{M}$.

These new data are also part of our continuing investigations of problems such as whether or not the characteristics of disks are the same around stars of different mass and, as the disks dissipate and angular momentum is transferred, how $\dot{M}$ decreases with age. Earlier papers in this series identified disk candidates in the Orion flanking fields using $U-V$ excesses (R00) and near-infrared ($I-K$ and $H-K$) excesses, as well as correlations of these disk indicators with rotation period (Rebull 2001, hereafter R01). A forthcoming paper (Makidon et al. 2002) will specifically address the relationship between disks and angular momentum for stars in the current sample in NGC 2264.

The analysis presented here parallels closely that found in R00 and R01. After describing the observations and data reduction (§ 2) and the basic observational results (§ 3), we discuss dereddening of the photometry (§ 4). Following that, we review the age and mass distributions (§ 5). We then discuss our selection of disk candidates (§ 6), based on Hα equivalent width, $I-K$ and $H-K$ excesses, and $U-V$ excesses. We arrive at mass accretion rates (§ 7), which we correlate with stellar mass and age. Finally, we summarize our major conclusions (§ 8).

Throughout the rest of this paper, we abbreviate I_C as simply I and, similarly, R_C as R. In addition, when discussing color excesses (particularly in § 6 on disk candidate selection), $U-V$ excess is abbreviated simply UV excess, $I-K$ excess abbreviated as IK excess, and $H-K$ excess as HK excess.

2. OBSERVATIONS AND DATA REDUCTION

In this paper, we present photometry obtained in *UBVRIJHK* for ~5600 stars and classification spectra for ~400 stars located within a $45' \times 45'$ field in NGC 2264; see Figures 1 and 2. Data are listed in Tables 1 and 2; derived quantities are given in Table 3. We summarize the distribution of photometric and spectroscopic data by wavelength in Table 4. Time series photometry was also obtained for this field using the University of Texas-McDonald Observatory's 0.76 m telescope; these light curves and their analysis will be discussed in Makidon et al. (2002). Existence of this supplemental data is relevant to the present paper since our spectroscopic sample was selected based on initial results from the time series.

In this section we discuss our spectroscopy (§ 2.1), our optical photometry (§ 2.2), and our near-infrared photometry (§ 2.4). In § 2.2 we also define the first of two subsets of the data used throughout the rest of this paper: "on-cloud," which is based on the physical projected position of a star compared with background dark cloud. The other term, "in-locus," is based on the position of a star in the color-magnitude diagram (see § 3).

2.1. *Spectroscopy*

We obtained moderate resolution ($R \sim 1000$, or 5 Å) classification spectra spanning the wavelength range 5000–9300 Å for a sample of 399 stars using the WIYN[10] 3.5 m and the Hydra fiber-optic echelle in queue mode during the fall of 1996 and the fall of 1997 observing seasons. This spectroscopic sample was selected primarily from a list of variable stars with amplitudes $\geq$0.02 mag discovered from initial analysis of an I-band time series study (Makidon et al. 2002). Of the 399 stars with spectra, 176 are variable, with the distribution of standard deviations in their light curves strongly peaked at $\sigma \sim 0.03$ and a tail extending to $\sigma \sim 0.25$ mag. Of the variable stars, 98 are periodic and 78 are aperiodic within our periodicity detection limits of ~0.1–25 days. The remainder of the spectroscopic sample includes objects with previously reported x-ray or Hα emission, likely proper-motion membership, and bright stars projected onto the face of the NGC 2264 molecular cloud, which were observed to enable optimal use of the ~100 available Hydra fibers. For the nonvariables in our time-series photometry, the distribution of light-curve standard deviations is sharply peaked at $\sigma \sim 0.01$ (comparable to typical errors), with a tail extending to only $\sigma \sim 0.10$.

Eight fiber configurations were used, with three 10 minute exposures for the brighter stars and three half-hour exposures for the fainter stars. The standard IRAF[11] Hydra software pipeline DOHYDRA was used to process these data. The signal-to-noise ratio of each reduced spectrum depends on fiber placement and transmission, but is typically ~40. The limiting magnitude of this survey is $I \sim 14$–15.5.

We classified our spectra using the Allen & Strom (1995) classification standards, which are specifically intended for this spectral range and resolution, supplemented by the Kirkpatrick, Henry, & McCarthy (1991) late-M standards. Three of the authors independently classified each star, and the resultant lists were combined to determine the most likely spectral type for each star. We have unambiguous classifications for 366 stars, and we use them for the spectroscopic analysis in this paper. Ranges in spectral type for the remaining 33 stars are reported in Table 2 but are not used in the analysis. We estimate the classification accuracy at two subclasses for the earliest types (A, F, and G), one subclass for the K stars, and less than a subclass for the M stars. The origins and effects of classification errors have been discussed by R00 and Hillenbrand (1997).

Hα equivalent widths were measured for all stars in our spectroscopic sample using the fitting algorithms incorporated in the IRAF task SPLOT. Uncertainties in the reported equivalent widths were estimated both from independent measurements of the same spectra and by comparison between repeat measurements of the few stars for which we obtained multiple spectra. For the most probable spectral type among our sample (M1), the uncertainty in W(Hα) is typically 20%.

[10] The WIYN Observatory is a joint facility of the University of Wisconsin-Madison, Indiana University, Yale University, and the National Optical Astronomy Observatory.

[11] IRAF is distributed by the National Optical Astronomy Observatory, which is operated by the Association of Universities for Research in Astronomy, Inc., under cooperative agreement with the National Science Foundation.

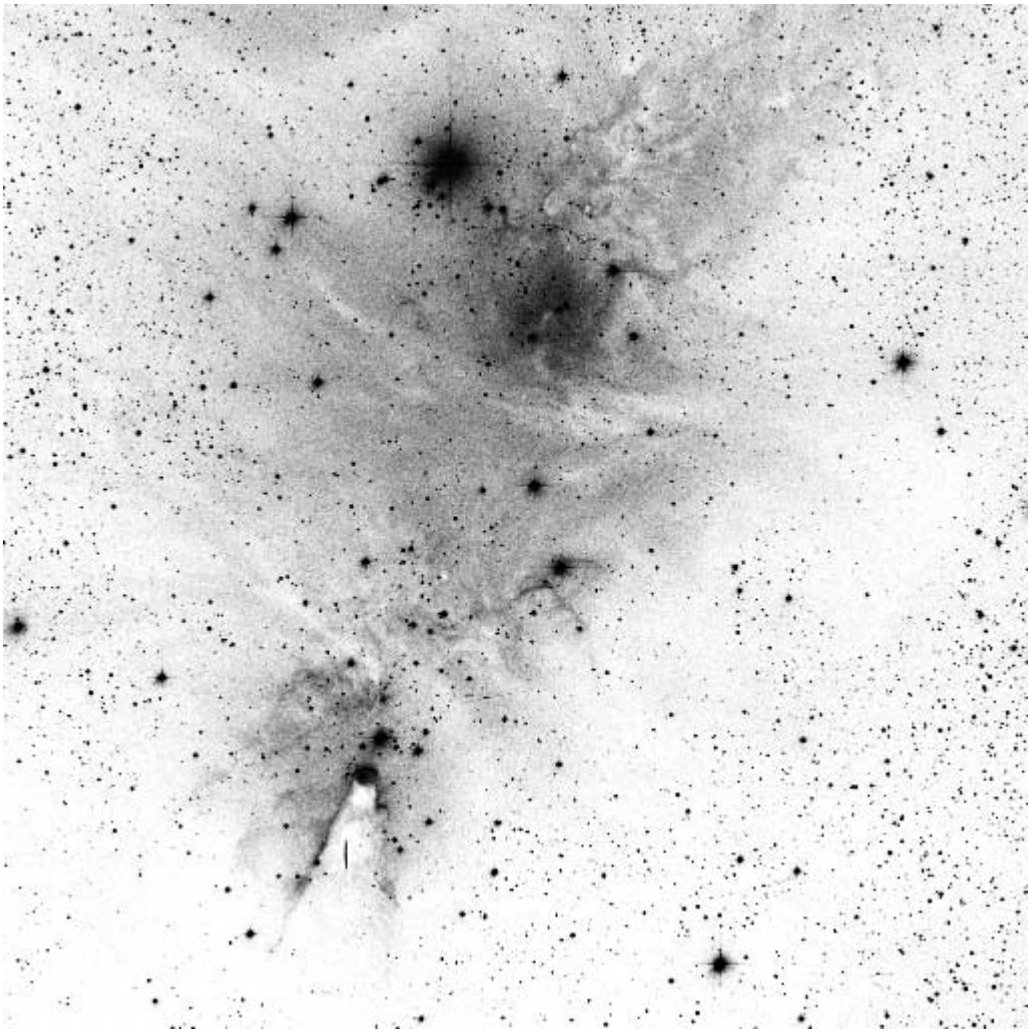

FIG. 1.—Digitized Sky Survey images (from STScI) illustrating the placement of our 45′ × 45′ NGC 2264 field. North is up, and east is to the left. Time-series photometry for these stars will be presented in Makidon et al. (2002). Optical photometry and spectroscopy are discussed in the present paper.

2.2. *Optical Photometry*

We obtained *UBVRI* (Johnson *UBV* and Kron-Cousins *RI* systems) observations of our field with the McDonald 0.76 m on the night of 1997 January 30, using the f/3.0 prime focus corrector and a 2048 × 2048 Loral Fairchild CCD, with a pixel scale of 1.″355 pixel^{-1}. To provide adequate cosmic-ray rejection, we acquired three 900 s exposures of the field in *U* and four 300 s exposures in *B* while the cluster was at minimum air mass. To avoid saturation of the bright stars at the longer wavelengths, we obtained two exposures in each filter: 45 and 450 s exposures in *V*, 45 and 300 s exposures in *R*, and 30 and 300 s exposures in *I*. The total time differential between the first and last observations in this *UBVRI* snapshot set was 2.75 hr.

We interspersed observations of the NGC 2264 field with observations of the Landolt standard fields SA-95 and SA-98 (Landolt 1992) in all filters at a variety of air masses and exposure times. We chose these standard fields both for their relative closeness to NGC 2264 and for the number of

TABLE 1

OBSERVATIONS I: OBSERVATIONS OF THE ON-CLOUD AND IN-LOCUS STARS

Star	R.A.	Decl.	I	σ_I	$U-B$	$B-V$	$V-R$	$R-I$	K	$J-K$	$H-K$	Type	A_I	A_V
3	06 39 15.3	+09 39 37.7	12.45	0.01	1.11	1.84	1.04	1.05	...	...	...	...	...	...
319	06 39 25.3	+09 40 08.6	11.79	0.01	1.05	2.23	1.28	1.29	...	...	...	...	...	...
353	06 39 24.0	+09 42 01.5	13.06	0.01	...	2.56	1.47	1.47	...	...	...	...	...	...
426	06 39 25.5	+09 36 46.4	15.88	0.01	...	1.72	...	...	...	...	...	...	...	...
436	06 39 25.9	+09 38 12.3	14.38	0.01	1.11	1.46	0.92	0.96	...	...	...	K7	0.73	1.20

NOTES.—Table 1 is presented in its entirety in the electronic edition of the Astronomical Journal. A portion is shown here for guidance regarding its form and content. Units of right ascension are hours, minutes, and seconds, and units of declination are degrees, arcminutes, and arcseconds. Coordinates are J2000.0, good to at least ∼1″, except for stars detected only in *JHK*, where coordinates are limited by the registration of the various individual SQIID frames to be ∼2″ (see text).

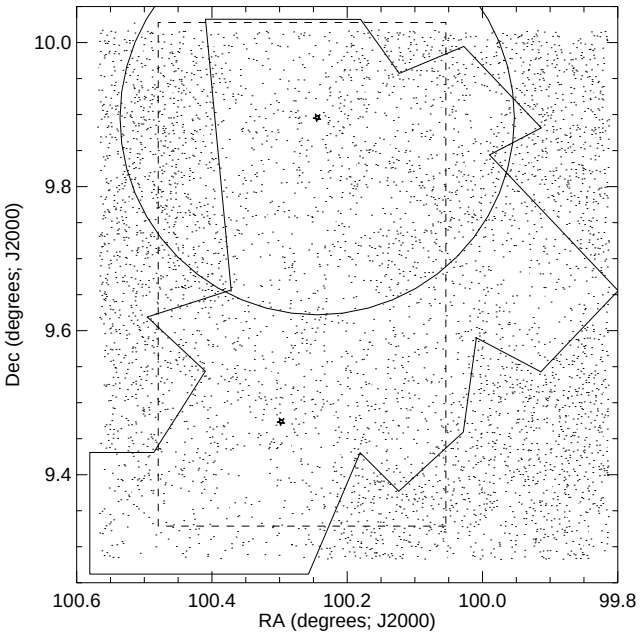

FIG. 2.—Representation of the field coverage of our optical survey (*dots*), near-infrared survey (*dashed line*), the region covered by the proper motion study (*thin line, large circle*), and the region defined as "on cloud" (*irregular polygon*). S Mon (HD 47839) is plotted as a star in the northern half, and HD 47887 (the B star powering the Cone Nebula) is plotted as a star in the southern half.

calibration stars available in each field. Typically, we were able to extract photometry for 20 or 30 calibration stars in each field.

Standard IRAF procedures were used for bias subtraction and flat fielding, with the addition of a shutter-correction algorithm employed for the short (<1 minute) exposures. We performed simple aperture photometry on all our frames using the IRAF task DAOPHOT, employing the same aperture size and sky annuli for both the Landolt fields and NGC 2264 fields since they were obtained together. While a few of the stars in our NGC 2264 fields have close apparent companions, the stellar density is generally low enough to make aperture photometry acceptable.

Quoted photometric uncertainties are a combination of photon noise, calibration uncertainties (owing to air mass corrections and zero-point correction), and flat-field uncertainties. Formal net error on all but photon and CCD noise for most filters was ~0.01 mag. Measurements were retained in any filter or color if the aggregate errors were less than 0.15 mag. The most likely error is 0.01 mag for all the optical filters except the *U* filter, where the most likely error is 0.02 mag. Total numbers of stars and limiting magnitudes in each filter are reported in Table 4. Note that the largest errors (near 0.15 mag) are obtained for the stars nearest the limiting magnitude for each filter.

We compare our photometry to those of other recent investigators in Table 5, where we report the mean offsets (quoting statistical errors from scatter in the distribution) between our study and those of others. We find no significant variations in these numbers if only the redder or bluer stars are used for the comparison. Differences between the studies can be accounted for by slight differences in filters, different standards used, and/or intrinsic stellar variability.

The reference frame for the coordinates presented for the optical sample is that established by the USNO-A2.0 catalog (Monet et al. 1998); coordinates are good to at least ±1″ over most of our field.

TABLE 2

OBSERVATIONS II: SPECTRAL TYPES OF OFF-CLOUD OR NOT-IN-LOCUS STARS

Star	R.A.	Decl.	Type
34	06 39 16.0	+09 26 52.1	F3
99	06 39 17.7	+09 33 26.2	K0
105	06 39 17.9	+09 30 43.4	K1
177	06 39 19.6	+09 31 11.5	M1
181	06 39 19.7	+09 26 49.7	G5

NOTES.—Table 2 is presented in its entirety in the electronic edition of the Astronomical Journal. A portion is shown here for guidance regarding its form and content. Coordinates are J2000.0, good to at least ~2″.

2.3. *Proper Motions*

Preliminary proper motions were determined from nine first epoch plates taken in 1960–1961 and nine second epoch plates taken in 1981–1983 with the Lick Shane 3 m reflector. The plates were taken at prime focus with the corrector in place and measured on the Lick Automatic Measuring Engine. The measurements were reduced for proper motion using a central overlap algorithm (Jones & Walker 1988), and the proper motions were used to determine membership probabilities, using the technique described in Jones & Walker. The errors in the proper motions were typically 1 mas per year in each coordinate. New CCD images were obtained with the Shane telescope in 2000 December, effec-

TABLE 3

OBSERVATIONS III: DERIVED PARAMETERS FOR ON-CLOUD AND IN-LOCUS STARS WITH SPECTRA

Star	UV Excess	IK Excess	HK Excess	Hα (Å)	Mass ($M_\odot$)	log (age/yr)	Radius ($R_\odot$)	log ($\dot{M}/M_\odot$/yr)
436	−0.63	...	...	...	0.64	6.0	1.77	−8.90
453	−0.62	...	...	−1.09	0.67	6.0	1.82	−8.31
908	−0.62	...	...	57.47	0.84	6.5	1.44	−8.41
987	0.09	...	...	−3.32	1.64	6.8	1.96	...
1052	−0.32	...	...	4.63	0.40	6.1	1.48	...

NOTE.—Table 3 is presented in its entirety in the electronic edition of the Astronomical Journal. A portion is shown here for guidance regarding its form and content.

TABLE 4
OBSERVATION SUMMARY

Filter (1)	No. Stars (2)	No. On-Cloud (3)	No. On-Cloud and In-Locus (4)	Limiting Magnitude (5)
U	1287	409	303	$U = 19.6, I = 15.5$
V	2792	938	650	$V = 18.8, I = 16.6$
R	4014	1518	650	$R = 18.5, I = 17.5$
I	4973	2103	682	$I = 17.9$
UVI	1287	409	303	$I = 15.7$
JHK	1628	1307	441	$J = 14.7, H = 14.1, K = 13.9, I = 14.7$
UBVRIJHK	380	272	216	$I = 14.6$
Membership[a]	1264	792	199	$I = 17.1$
Spectral types	366	247	210	$I = 14$–15.5
UVI and types	245	150	138	$I = 14$–15.5
Total[b]	5607	2613	682	

[a] Membership in this context means stars with preliminary proper-motion membership probabilities ≥ 0.85.
[b] "Total" refers to total number of unique stars in each column: (2) all stars; (3) on-cloud; (4) and on-cloud and in-locus.

tively doubling the epoch span, and the proper motions and membership are currently being redetermined.

The proper motions cover a circular region centered on S Mon, not covering our whole field (see Fig. 2). From this sample, we accepted as candidate members anything with a preliminary membership probability ≥ 0.85. Specifically because we do not have preliminary membership probabilities for stars over our whole field (or to the depth of our survey), we defined a region to be "*on-cloud*" via studies of the surface density of stars and a determination of the $A_V = 5$ boundary; see Figure 2. There are 1265 stars with preliminary membership information, 792 (62%) of which are on-cloud. Of the on-cloud sample, there are 258 with preliminary membership probabilities ≥ 0.85, leaving 534 nonmembers (33% members, 67% nonmembers). Off-cloud, there are 81 members and 392 nonmembers (17% members, 83% nonmembers). We take these numbers as evidence that our on-cloud approximation limits our sample more effectively to actual cluster members. We refine this approximation further in § 3, when we define the locus of stars in the color-magnitude diagram.

2.4. *Near-Infrared Photometry*

We obtained *JHK* observations with the SQIID camera in 1993 January on a six-night run at the KPNO 1.3 m telescope. In order to tile over the region depicted in Figure 2, 49 separate pointings were required. Frames were overlapped to create a mosaic using the software packages developed for SQIID by K. Merrill (1993, private communication). A global astrometric solution for the final mosaic yielded positions good to $\pm 2''$, limited by the registration of the individual frames.

Processing was completed in the same fashion as described in Hillenbrand et al. (1998). Calibration to the standard system was accomplished (1) by comparison with *JHK* photometry obtained in 1991 using the single-channel InSb photometer (OTTO) on the KPNO 1.3 m; and (2) via adoption of transformations obtained with SQIID during the 1993 January run. The formal uncertainties in the OTTO/SQIID comparisons for 53 stars in common are ± 0.05 mag in *H* and *K*, and ± 0.07 mag in *J*. These uncertainties are a result both of the effects of undersampling inherent to the SQIID data and intrinsic variability of the sources. The uncertainties in the transformation to the standard system using the SQIID data alone are estimated to be ± 0.03 mag in all colors.

Photometry in all three bands was obtained for 1628 objects; stars with detections in only one or two bands were omitted from the final list. The approximate completeness limits of our survey are in Table 4 and are consistent with those in Strom, Strom, & Merrill (1993), where the data were taken using similar protocols.

We looked for optical counterparts based on positional matches within $2''$. There are 634 objects for which no optical counterparts were obtained. Most of these near-IR–only objects can be explained by one or more of the following: (1) the object is near the edge of a SQIID frame, so the astrometry is clearly worse than the mean; (2) the object is near a star or nebulosity, which is bright and/or saturated in the optical frames (so no optical measurements could be obtained); or (3) the object is clearly very red, which we infer to mean it is so deeply embedded in molecular material that no optical counterpart would be expected. These stars without optical counterparts are listed in Table 1; but note that they have larger position uncertainties ($\pm 2''$) than those stars with optical detections.

TABLE 5
COMPARISON OF OPTICAL PHOTOMETRY: MEAN OFFSETS

Investigation	*I*	*U*−*B*	*B*−*V*	*V*−*I*
Park et al. 2000	-0.019 ± 0.008	-0.086 ± 0.016	0.076 ± 0.005	0.023 ± 0.005
Flaccomio et al. 1999	-0.087 ± 0.005	...	0.100 ± 0.008	0.144 ± 0.006
Sung et al. 1997	0.017 ± 0.003	0.000 ± 0.009	0.044 ± 0.003	0.006 ± 0.002

NOTE.—These values represent mean offsets between the present study and the literature studies; errors represent scatter about that offset.

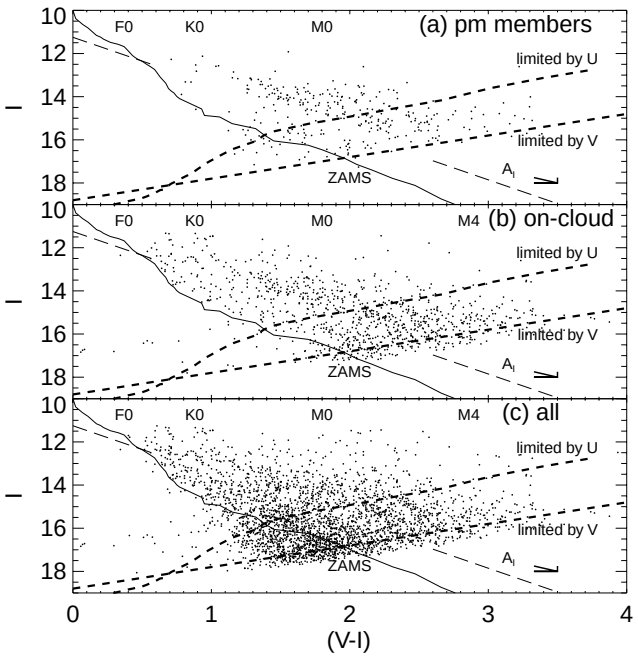

FIG. 3.—Observed CMDs for (*a*) stars with V and I measurements that are also candidate proper-motion member stars (probability ≥ 0.85); (*b*) stars from the on-cloud sample with V and I measurements; (*c*) all stars with V and I measurements. The ZAMS (*solid line*) is indicated in each panel. Note the concentration of stars in a clump above the ZAMS, most obvious in the first panel and most subtle in the last. The line defining this locus (*long dash*) was determined in (*a*) and is meant to run continuously from upper left to lower right, but has been plotted as line segments to better allow the reader to assess the distribution of stars in the diagrams. The fact that the likely field star contamination is greatly reduced in (*b*) compared with (*c*) and that the locus structure that is found in the much more limited (in space and mass) sample plotted in (*a*) is also found in (*b*) reassures us that the on-cloud approximation is indeed preferentially selecting cluster members. The reddening vector for $A_I = 0.25$ ($A_V = 0.41$) and $E(R-I) = 0.10$ [$E(V-I) = 0.17$] is included in the lower right. Short-dashed lines are the completeness limits in U and V, calculated using our measured sensitivity combined with main-sequence colors.

3. BASIC OBSERVATIONAL RESULTS

In this section, we present a basic characterization of our database in the form of color-magnitude diagrams (CMDs) and color-color diagrams. The CMDs are used to define a subset of the data used throughout the rest of this paper, which we call "in-locus," a subsample likely dominated by cluster members. The color-color diagrams are used to illustrate the large fraction of disked objects in our sample. More detailed analysis of the stellar population as defined in the CMD and of the disked population appears in subsequent sections.

3.1. *CMDs: Characterizing the Stellar Population*

Figure 3 presents three CMDs in I and $V-I$. Figure 3*a* is the subset of candidate member stars based on proper motions, Figure 3*b* is the subset of on-cloud stars, and Figure 3*c* is the complete set of ~5600 stars with V and I measurements. These data have not been corrected for reddening, although a vector indicating the direction and slope of typical reddening (as derived in § 4) is shown for reference. The zero-age main sequence (ZAMS; shown from A0–M4) includes measurements from Bessell (1991), Leggett (1992), and Leggett, Allard, & Hauschildt (1998). We assumed a distance modulus of 9.40 (Sung et al. 1997; Park et al. 2000) for this study. We transformed the completeness limits of $U = 19.6$ and $V = 18.8$ into the I- and $V-I$-plane; however, because these transformations are based on ZAMS colors, stars fainter than this can be detected in our sample if they have photometric excesses at the shorter wavelengths due to, e.g., accretion.

First looking at the most general CMD, Figure 3*c*, there is clearly a large population of stars below the ZAMS. These are likely field stars; this cluster lies in the Galactic plane (Galactic coordinates 202.96, +2.22), so field-star contamination is expected. However, we noted above that there is a dark molecular cloud just behind the cluster. Figure 3*b* is just the on-cloud sample, and there are many fewer stars below the ZAMS in Figure 3*a* than in Figure 3*c*, which we interpret to mean that the Galactic contamination has been significantly reduced when working with just the on-cloud sample.

In Figure 3*a*, which is limited to those stars with preliminary proper-motion membership probabilities $\geq$0.85, the sample is dominated by stars in a clump centered ~2 mag above the ZAMS. In this panel in particular a gap between this stellar population and that closer to the ZAMS is apparent, similar to a gap found by R00 in Orion. In our analysis we defined a line separating the stars in the clump that are above the line (likely to be members of the cluster) from the stars below the line (likely to be field stars). Figure 3*b*, limited to the on-cloud sample, has a similar gap, and even Figure 3*c* has a barely discernible gap at the same location. This clump of PMS stars well above the ZAMS is hereafter referred to the cluster *locus*. Note that this definition is made in the observational (not dereddened) plane; subsequent investigation of the dereddened plane shows that the chosen line is both acceptable and accurate. Note also that we require V and I magnitudes to be able to place a star in or out of the locus, whereas the on-cloud sample is defined only by right ascension and declination.

Because we want to select those stars most likely to be cluster members, we analyze those stars found both on-cloud and in-locus when not otherwise specified in the remainder of this paper. One can justifiably ask how good this approximation is for the smaller subset of stars for which we have preliminary proper-motion membership information. There are 385 stars with preliminary proper-motion membership information that are also on-cloud, in-locus, and with $I \leq 17$; 199 of them (52%) are provisional members, and 186 (48%) are provisional nonmembers. Of the 191 stars with preliminary proper-motion membership information, off-cloud, not in the locus, and with $I \leq 17$, 80% are nonmembers, and 20% are members. We conclude that in the absence of a proper-motion membership survey over our entire field and to our limiting magnitude, we are making a reasonable approximation by taking as preliminary cluster members those stars both on-cloud and in-locus. It is this sample that is carried forward through our detailed analysis steps.

3.2. *Color-Color Diagrams: A First Look at the Disk Candidates*

Figure 4 presents three observed $U-V$ and $V-I$ color-color diagrams; in analogy to Figure 3, Figure 4*a* is the subset of candidate proper-motion member stars, Figure 4*b* is the subset of on-cloud stars, and Figure 4*c* is the complete set of 1287 stars with UVI measurements. These data have

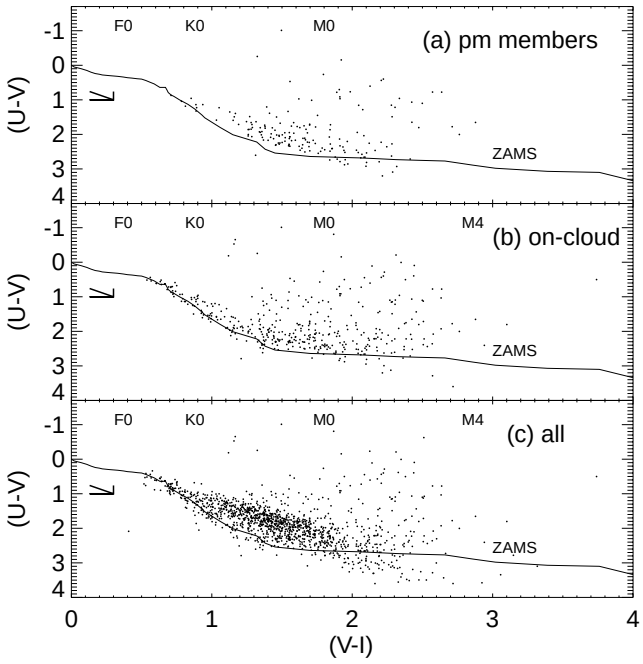

FIG. 4.—Observed $U-V$ vs. $V-I$ color-color diagrams for (*a*) stars with *UVI* measurements that are also candidate proper-motion member stars (probability ≥ 0.85); (*b*) stars from the on-cloud sample with *UVI* measurements; (*c*) all stars with *UVI* measurements. The ZAMS relation and a sample reddening vector are indicated. Note the substantial population of stars much brighter than expected in $U-V$, whose positions cannot be explained by reddening.

not been corrected for reddening, although a vector indicating the direction and slope of typical reddening (as derived in § 4) is shown for reference. Figure 5 presents the observed $U-V$ and $V-I$ color-color diagram for just the on-cloud and in-locus stars with *UVI* photometry. In each of these plots, there are a few stars located below the ZAMS relation which can be dereddened to intersect the ZAMS. Our focus for this paper, however, is on the many stars located high enough in this diagram that they cannot be dereddened to intersect the ZAMS; these are the $U-V$ excess stars. Note that in Figures 4*a* and 4*b*, the fraction of stars with very large UV excesses (larger than -1.1 mag) is constant and much greater than the fraction of similar stars in Figure 4*c*. We interpret this as support for our hypothesis that the on-cloud sample represents a population likely to be cluster members.

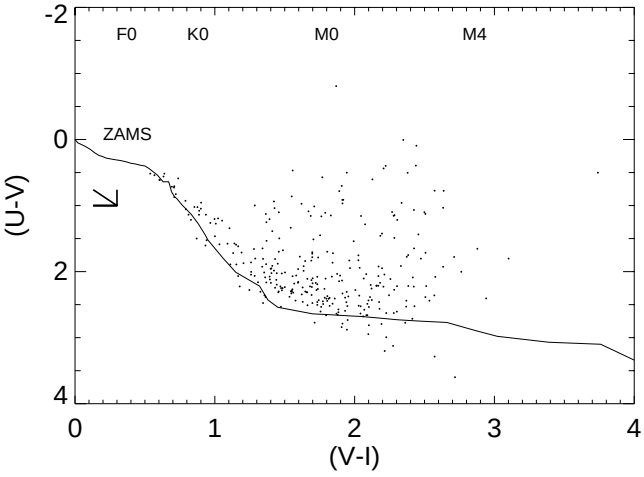

FIG. 5.—Observed $U-V$ vs. $V-I$ for on-cloud and in-locus stars. The ZAMS relation and a sample reddening vector are indicated. Note the substantial population of stars much brighter than expected in $U-V$, whose positions cannot be explained by reddening.

Figure 6 presents the observed $J-H$ versus $H-K$ and $H-K$ versus $R-I$ color-color diagrams. These data have not been corrected for reddening, although dotted lines indicating the direction and slope of typical reddening (as derived in § 4) is shown for reference. Note the substantial population of stars much redder than expected in $H-K$, whose positions cannot be explained by reddening; in Figure 6*a*, 22% of the stars are redder than expected in $H-K$, and in Figure 6*b*, 18%. We will discuss these red stars in more detail in § 6 below.

3.3. *CMDs: Characterizing the Spectroscopic Population*

In addition to the photometry just discussed, we have optical spectroscopy for 366 of the stars in Figures 3 and 5, selected primarily on the basis of temporal variability and/or previous designation as a young stellar object. In § 4 we will combine the spectra and the photometry to derive individual extinction values, as well as the modal or most likely reddening. Figure 7 shows a histogram of our spectral types. M stars compose 42% of the sample, and K stars 35%. There are 210 of those stars located both on-cloud and in-locus, 107 (51%) of which are M stars, and 78 (37%) are K stars.

We can ask (retroactively since the spectroscopic sample was selected based on preliminary variability data and before the *UBVRIJHK* photometric database was completed) the degree to which our spectroscopic sample represents our photometric sample of candidate NGC 2264 members (on-cloud and in-locus). We answer this question by comparing the location of stars from each sample in the color-magnitude diagram. Figure 8*a* highlights the stars with spectroscopy in the CMD for the on-cloud sample (with a line drawn to indicate the in-locus sample). This figure suggests that the photometric and spectroscopic populations generally cover the same regions of the CMD, but there is a strong bias of the spectroscopic sample toward the in-locus sample. This bias confirms that our selection of candidates for spectroscopy based on photometric variability has preferentially selected young candidate members of NGC 2264 and subsequently reinforces our belief that the locus population is more likely to be comprised of bona fide members of NGC 2264. The issue of variability and membership will be discussed more in Makidon et al. (2002).

Figure 8*b* shows the fraction of stars with spectral types as a function of $V-I$ for just the stars on-cloud and in-locus. The sample is complete in color between $V-I \sim 0.7$–2.4. Between $V-I \sim 1$ and $\sim$2.2, the spectroscopic sample represents an approximately constant fraction of the photometric sample. Outside these limits the spectroscopic sample is clearly less uniformly representative. As in R00, however, this is not a critical point, given that one of our primary goals is to derive mass accretion rates as a function of mass and age, not to derive the mass and age distributions.

4. REDDENING CORRECTIONS

As in R00, we start by deriving the interstellar reddening and extinction [measured here as $E(R-I)$ and A_I] toward each star in our sample. This can be done on an individual

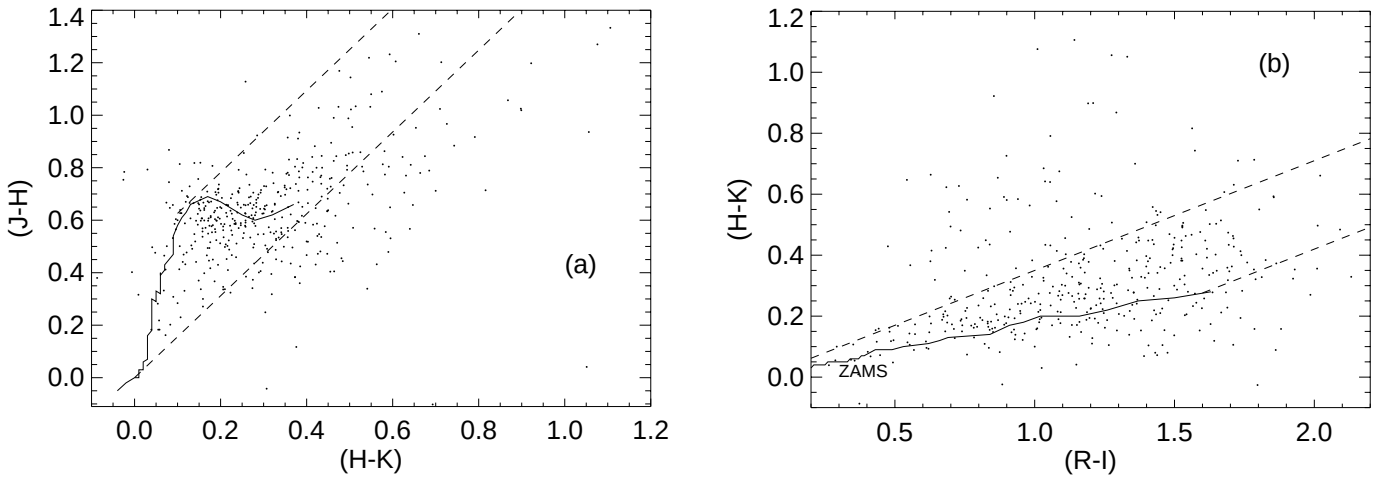

FIG. 6.—(*a*) Observed $J-H$ vs. $H-K$ and (*b*) observed $H-K$ vs. $R-I$ diagrams for on-cloud and in-locus stars. In both panels the ZAMS relation is indicated, as is the slope of the reddening vector (*dashed lines*). Note the substantial population of stars much redder than expected in $H-K$, whose positions cannot be explained by reddening.

basis for those stars with both photometry and spectroscopy. We compare observed stellar colors with those expected based on spectral classification to obtain estimates of color excesses. We use the wavelengths at which the contribution from nonphotospheric (i.e., circumstellar) sources is minimized, which is the color index $R-I$. Dereddening relationships we use are for $R = 3.1$ (Fitzpatrick 1999; Mathis 1990). The expected photospheric colors include measurements from Bessell (1991), Leggett (1992), and Leggett et al. (1998).

Figure 9 shows histograms of $E(R-I)$ and A_I. When considering any of the subsets of data (on-cloud, in-locus, preliminary proper-motion members) these histograms are statistically identical, so all stars are included here to improve the statistics. As in R00, there are some stars (56, or 15%) that have apparently negative reddening. This sample, however, has fewer of these problem stars than R00, possibly because here we are able to use $R-I$ rather than $V-I$ for dereddening, where the change in color between spectral types is less steep. We refer to R00 for extensive discussion of these issues and note that the A_I most appropriate to use in the absence of other reddening information is the modal, or most likely, value from Figure 9, rather than the mean or median A_I. We take as the most likely values $E(R-I) = 0.10 \pm 0.02$ and $A_I = 0.25 \pm 0.15$ ($A_V = 0.41$); errors on these numbers are derived from the widths of the histograms in Figure 9.

Other investigators have also derived low values of reddening toward members of this cluster. Sung et al. (1997) find $E(B-V) = 0.071 \pm 0.033$ from 21 stars, while Park et al. (2000) derive $E(B-V) = 0.066 \pm 0.034$ from nine stars.

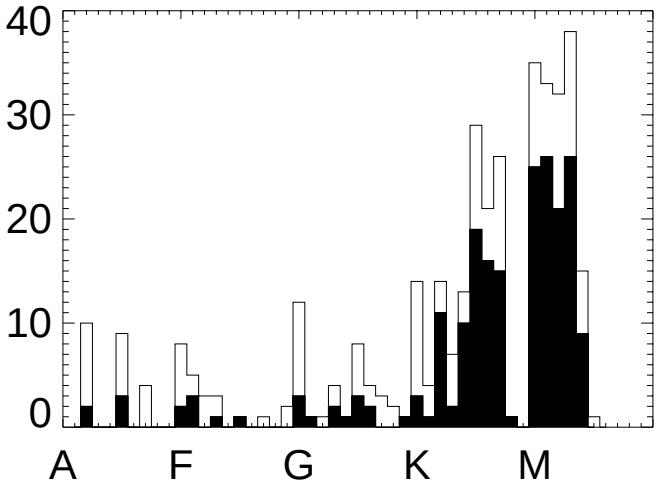

FIG. 7.—Histogram of all spectral types reported here for 366 stars in NGC 2264 (*line*) and just for those both on-cloud and in-locus (*filled histogram*). K stars are about 35% of both samples; M stars are 42% of the complete set, and 51% of the on-cloud and in-locus sample.

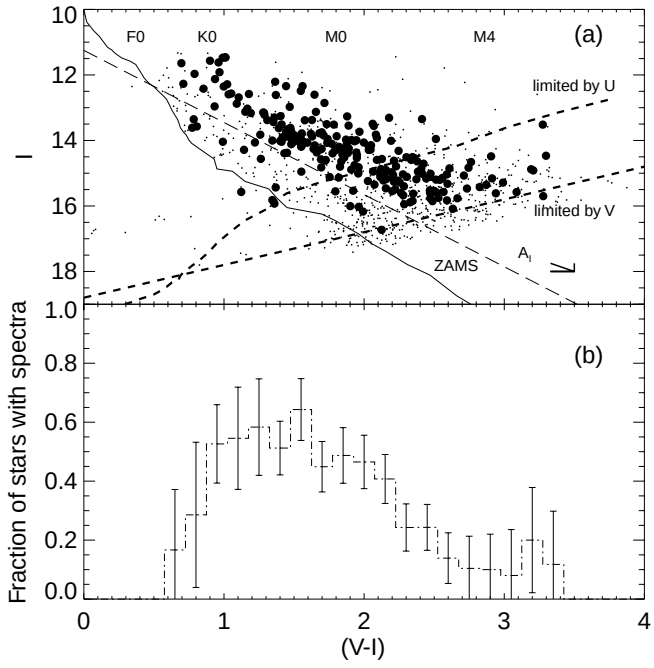

FIG. 8.—(*a*) CMD with on-cloud stars; stars with spectral types are indicated as large filled circles; all other notation is as in Fig. 3. (*b*) Fraction of on-cloud and in-locus stars with spectra as a function of $V-I$. Between $V-I \sim 1$ and ~ 2.2, the spectroscopic sample represents an approximately constant fraction of the photometric sample. Furthermore, the spectroscopic sample is largely in-locus despite being selected based on variability characteristics, not CMD location.

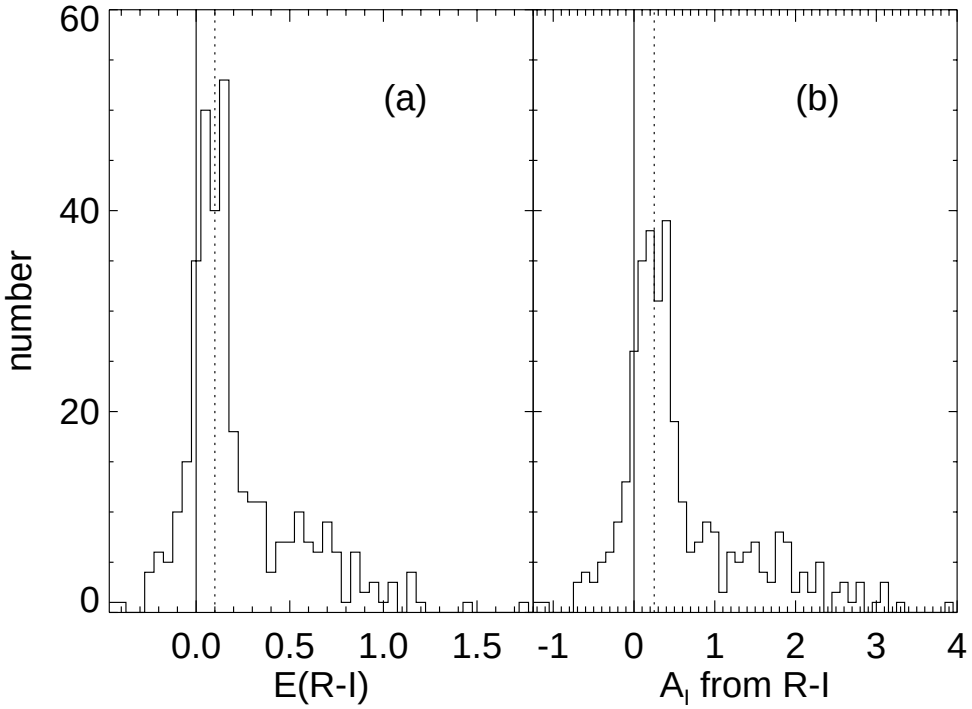

FIG. 9.—Histogram of (*a*) $E(R-I)$ and (*b*) subsequent derived A_I; a solid vertical line is placed at 0 for reference, and the dotted vertical line indicates the mode, or most likely value, selected for the analysis sections of this study, $E(R-I) = 0.10 \pm 0.02$ and $A_I = 0.25 \pm 0.15$ ($A_V = 0.41$).

Converting our most likely value of $E(R-I)$, we estimate $E(B-V) = 0.146 \pm 0.03$, a tenth of a magnitude larger than the Sung et al. result. Sung et al. and Park et al. both derived reddening using only a small number of O and B stars. We note that our reddening estimate is derived mainly from K and M stars—only 22% of the stars in our spectroscopic sample are earlier than K0. We find no dependence of reddening on the observed or intrinsic color, though we are constrained by small-number statistics for stars earlier than K0. Since the other recently published investigations considered only smaller regions contained within our $45' \times 45'$ field, we investigated the prospects for spatial variations in reddening. We find no evidence for significant variations within the on-cloud region defined above. We also investigated the role of small systematic errors in our derived colors compared with those of other authors. The observed offsets have been summarized above in Table 5. While the offsets in $B-V$ are larger than expected a priori, the offset in $V-I$ is 0.02 mag. Hence we have no reason to expect significant systematic uncertainties in the $R-I$ colors used to derive reddening. We conclude that the differences in derived reddening between our study and previous studies likely can be accounted for by the small number of and much earlier type of stars used by previous studies, combined with small instrumentation, calibration field, and filter differences; we note that the assumed photospheric colors may be a factor as well. Nonetheless, offsets at these level do not affect our subsequent discussion. Were the full 0.10 mag difference in $E(B-V)$ accounted for by a systematic error, the net affect on A_I would be 0.2 mag, resulting in an offset of 0.08 in log L.

We follow R00 closely for the rest of this investigation in that we carry forward two parallel analyses: one for the spectroscopic sample (limited to on-cloud and in-locus, and dereddened by values specific to each star); and the other for the complete set of stars (also on-cloud and in-locus, but dereddened using the most likely value of the extinction), called the "ensemble." In the later analysis the small amount of reddening found in this section to characterize the cluster as a whole is applied to the entire photometric sample in order to increase the number of stars under discussion (a common practice in the study of open clusters). In the former analysis, for those few stars with spectra and apparently negative reddening, we assume the most likely reddening value.

Figure 10 is the CMD for all stars with spectra, dereddened on a star-by-star basis (with the on-cloud and in-

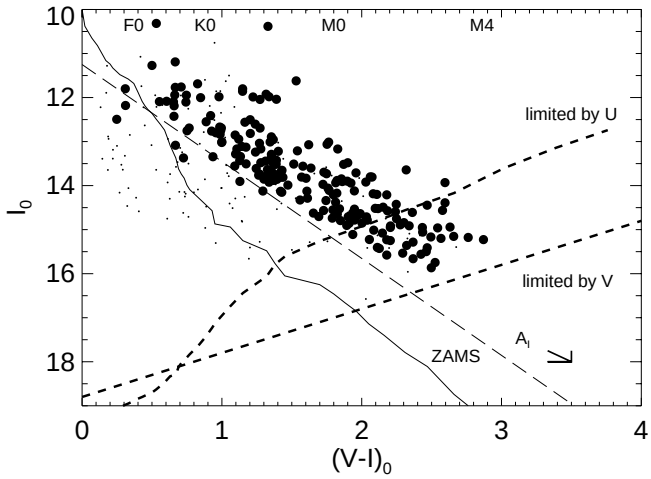

FIG. 10.—Dereddened CMD for the spectroscopic sample. Notation is as in Fig. 3, except the larger symbols correspond to the on-cloud, in-locus subsample. Some of the in-locus sample stars appear below the long dashed line, because the locus population is defined in the observed, not dereddened, plane.

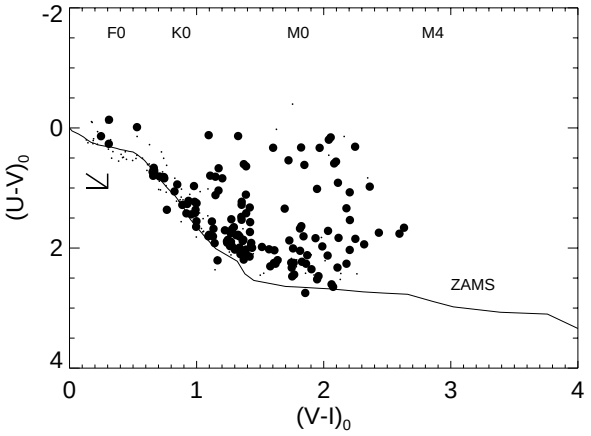

FIG. 11.—Dereddened $U-V$–$V-I$ color-color plot of the spectroscopic sample. Notation is as in Fig. 5, except the larger symbols correspond to the on-cloud, in-locus subsample. There are many stars which are substantially bluer in $U-V$ compared with ZAMS counterparts, an effect which was apparent even before the reddening corrections.

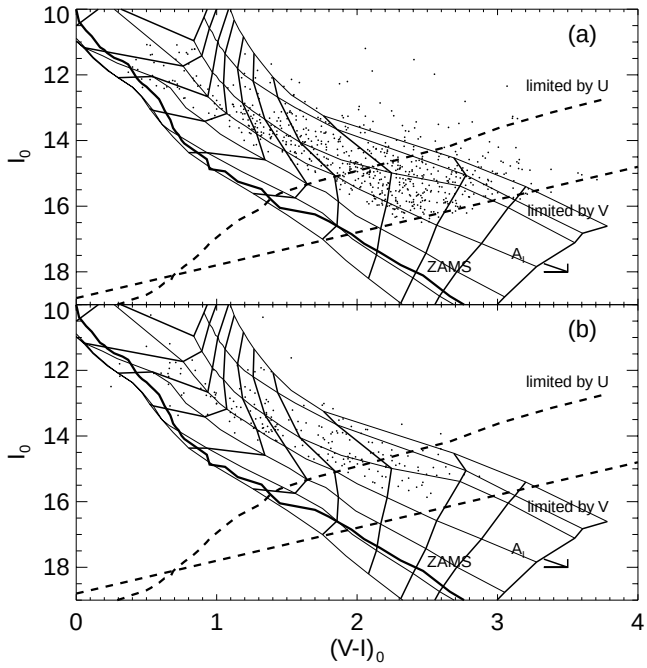

FIG. 12.—Dereddened CMD of (*a*) ensemble and (*b*) spectroscopic stars, with DAM Model 1 isochrones and lines of constant mass (0.1, 0.3, 1, 3, 10, 30, and 100 Myr; 0.1, 0.15, 0.2, 0.3, 0.5, 0.7, 0.9, 1.2, 1.5, 2.0, and 2.5 $M_\odot$). All other notation is as in Fig. 3. The intersection of the dashed detection limits and DAM model grid lines result in complicated completeness limits in terms of stellar mass and age; see text. Note that, in keeping with the framework established in earlier sections, both of these panels are limited to the on-cloud, in-locus subsample.

locus population indicated). In R00 stars were dereddened with $V-I$, resulting in an apparent quantization in the analogous figure. However, in this case, since we used $R-I$ to obtain the reddening values, there is no apparent quantization. Separately, the ensemble of all photometry was dereddened by the most likely value of reddening; this CMD is not reproduced here as it is identical to Figure 3, shifted by the most likely reddening vector as presented there.

Figure 11 shows the dereddened $(U-V)$–$(V-I)$ color-color diagram for the spectroscopic sample. A plot of the complete set of photometry dereddened by the most likely reddening is not presented, as it is essentially identical to Figure 5 There are many stars that are substantially bluer in $U-V$ compared with ZAMS counterparts, an effect that was apparent even before the reddening corrections.

5. AGE AND MASS DISTRIBUTIONS

The purpose of this section is *not* to derive definitive mass and age distributions, since selection effects and minimal membership information prohibit that. Rather, we aim to understand the *range* of masses and ages sampled by our data set.

The models most often used in the analysis of PMS stars are those of D'Antona & Mazzitelli (1994, hereafter DAM; Canuto & Mazzitelli convection prescription and Alexander opacities). We use these models to calculate the isochrones and lines of constant mass plotted along with our dereddened data in Figure 12, so as to enable direct comparison with previous analyses including R00, R01, and Hillenbrand (1997). Note that the ZAMS relation constructed from tabulated M_V and $V-I$ values does not align well with the oldest isochrone. This is a result of a variety of factors, the largest likely being inaccuracies in models, since the discrepancy seems to remain under many different plausible transformations from the theoretical to the observational plane. We use the transformation from Hillenbrand (1997) and interpolate stellar masses and ages in the observational plane. We are, of course, unable to derive masses and ages for stars outside the grid, and hence we cannot assign masses and ages for 82/650 (13%) stars in the ensemble photometric sample and 13/202 (6%) stars in the spectroscopic subset.

Siess, Dufour, & Forestini (2000, hereafter SDF)[12] have recently published models of PMS evolution. Stars with identical positions in the CMD can produce DAM masses a factor of 2 different from SDF masses and an order of magnitude different in age. Figure 13 compares masses and ages for DAM and SDF models (for the spectroscopic subset). Because many previous and current studies use DAM models, we continue to do so for the rest of this paper. The reader should keep in mind that differing ages and masses can be obtained via use of different models; see also Park et al. (2000).

As in R00, the combination of survey limits and the locus cut in the CMD results in complicated selection effects, as can be seen in Figure 12. In R00 the locus cut limited the age distribution to 3 Myr; the limit here is slightly older, at 6 Myr. The low-mass limit is higher than found in R00, a result of the greater distance of NGC 2264. We define ranges of completeness in mass and age analogous to those found in Figures 11 and 12 of R00; see our Figures 14 and 15. For the sample with U, V, and I magnitudes we derive completeness limits of 0.1–6 Myr and 0.6–2 $M_\odot$. Restricting the sample to 0.1–1 Myr enlarges the mass completeness range to 0.35–2 $M_\odot$. Working just with the sample with V and I magnitudes, the ranges are 0.1–6 Myr and 0.25–2 $M_\odot$. The spectroscopic subsample has effectively the same limits

[12] See http://www-laog.obs.ujf-grenoble.fr/activites/starevol/evol.html.

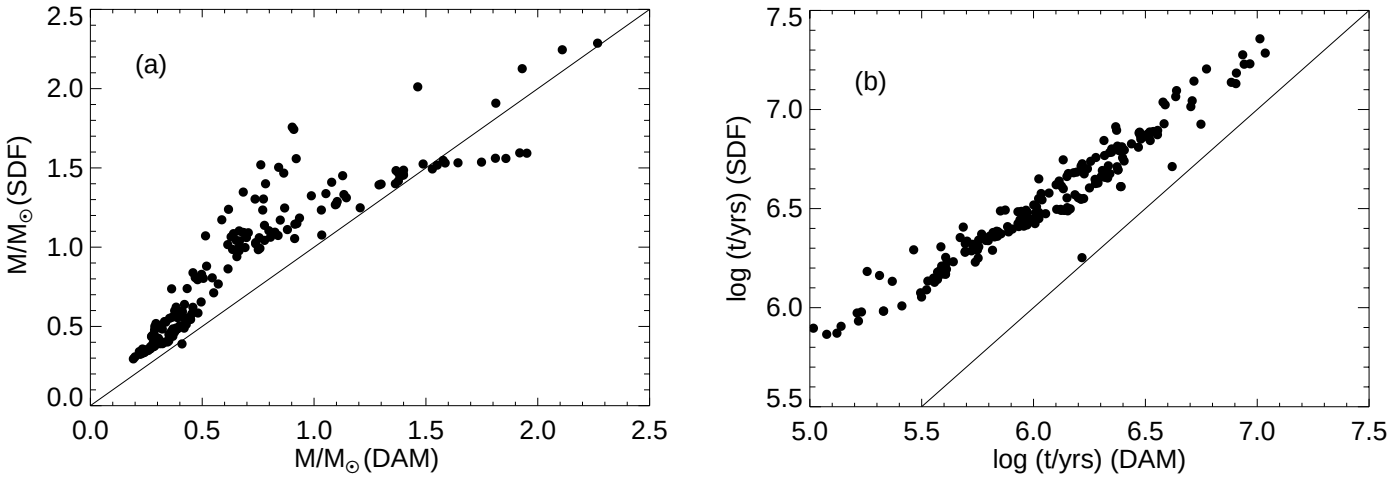

FIG. 13.—Comparison of (*a*) masses and (*b*) ages derived for the same stars (spectroscopic, on-cloud, and in-locus) via DAM and SDF. Lines indicate the 1 : 1 relationship along which masses and ages from the two models agree. Note that systematic differences in masses can be a factor of 2 and in ages can be half an order of magnitude.

as the subsample with U magnitudes. Since the reddening vector is essentially parallel to the isochrones, histograms of ages will be minimally affected by reddening uncertainties, while mass distributions will be moderately affected.

We note again that Figures 14 and 15 are not derivations of the true mass function of the cluster, but rather an indication of the range of masses and ages covered by our data. This range is comparable to that covered by R00, except that the NGC 2264 survey probes systematically slightly higher masses owing to its greater distance (0.15–3 $M_{\odot}$, compared with 0.12–2.5 $M_{\odot}$ in R00). For ages $\lesssim$3 Myr, the age distributions for the two clusters are statistically indistinguishable, a somewhat surprising result given that NGC 2264 is thought to be slightly older, at $\sim$3 Myr (Sung et al. 1997) compared with Orion, at $\sim$1 Myr (Rebull et al. 2000; Hillenbrand 1997). However, we note that we do not have extensive cluster-membership information for either cluster; in both cases we made a locus approximation in the CMD. Additionally, Sung et al. (1997) incorporate earlier stars than we do, and it is known that earlier PMS stars tend to show larger ages, presumably due to birthline effects (Hillenbrand 1997). We thus defer detailed comparison of age distributions in Orion and NGC 2264 to a later paper.

6. DISK CANDIDATE SELECTION

In this section we identify circumstellar disk candidates based on Hα (§ 6.1), near-IR color excesses ($I-K$ and $H-K$; § 6.2) and ultraviolet excesses ($U-V$; § 6.3), and we compare the efficiency of different disk indicators. Finally, § 6.4 summarizes this section. As above, if not otherwise specified, the subsample of stars discussed is that most likely to be bona fide members of the cluster, e.g., the union of the on-cloud and in-locus samples. Note also that $U-V$ excess is abbreviated as UV excess, $I-K$ excess as IK excess, and $H-K$ excess as HK excess.

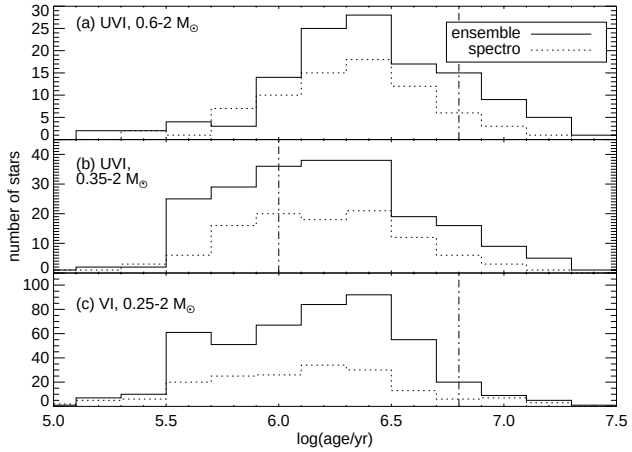

FIG. 14.—Histogram of DAM ages for each of the following data subsets: (*a*) *UVI* data with $0.6 < M/M_{\odot} < 2$, (*b*) *UVI* data with $0.35 < M/M_{\odot} < 2$, and (*c*) *VI* data with $0.25 < M/M_{\odot} < 2$. Solid lines are the ensemble, and dotted lines are the spectroscopic sample. Vertical dashed lines denote approximate completeness limits; data are most complete to the left of the lines.

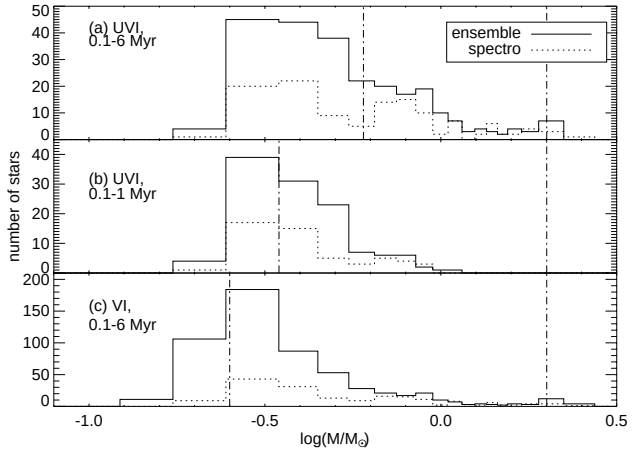

FIG. 15.—Histogram of DAM masses for each of the following data subsets: (*a*) *UVI* data between 0.1–6 Myr, (*b*) *UVI* data between 0.1–1 Myr (with slightly different completeness limits in mass), and (*c*) *VI* data 0.1–6 Myr. Solid lines are the ensemble, and dotted lines the spectroscopic sample. Vertical dashed lines denote approximate completeness limits; data are most complete between the two lines.

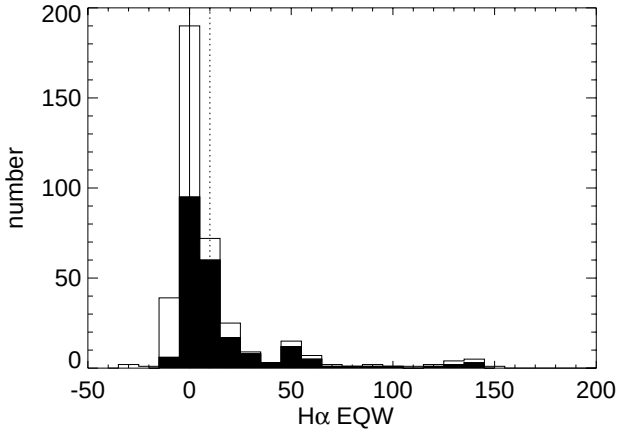

FIG. 16.—Histogram of Hα EQWs in angstroms, where positive EQW denotes emission. The plain histogram denotes the entire spectroscopic sample; the filled portion refers to subsample that is on-cloud and in-locus. Note that there are six stars with equivalent widths larger (in emission) than 200 Å. A vertical solid line has been placed at 0 Å EQW to guide the eye, and a vertical dotted line has been placed at 10 Å EQW to indicate the division between disk candidates (*to the right of the line*) and nondisk candidates.

6.1. Hα *Disk Candidates*

The most classical method of identifying active stars surrounded by disks has been from Hα emission. We present in Figure 16 a histogram of Hα equivalent widths, $W(\mathrm{H}\alpha)$. Superposed is a vertical line corresponding to $W(\mathrm{H}\alpha) = 10$ Å in emission, chosen to segregate stars likely to be surrounded by circumstellar accretion disks (stronger emission) from those that lack disks (Strom et al. 1990). It is believed that large Hα emission equivalent widths [$W(\mathrm{H}\alpha) > 10$ Å] reflect emission arising in magnetospheric columns, which transport material from the inner region of a circumstellar accretion disk to the stellar surface. Weaker Hα emission is believed to arise in active stellar chromospheres (Najita et al. 2000).

The demarcation between magnetospheric-dominated and chromospheric-dominated emission results from examination of the distribution of Hα emission equivalent widths among two samples in the Taurus-Auriga molecular clouds: those that have near-IR excesses, presumably diagnosing the presence of accretion disks and associated accretion along magnetospheric columns, and those that lack such excesses (e.g., Strom et al. 1990). Among this sample, dominated by stars with ages ~1 Myr and spectral types K5–M2, $W(\mathrm{H}\alpha) \sim 10$ Å provides a clean separation between stars with disks and no disks. Because our sample is dominated by stars of similar age and spectral type, we believe that adopting this simple criterion is reasonable.

However, we caution the reader that (1) among stars of ages ~1 Myr, the boundary between stars with and without disks will likely move to smaller equivalent width at earlier types (due to strong Hα absorption) and to larger width at later types (due to contrast effects); and (2) that among older stars the boundary may shift toward larger $W(\mathrm{H}\alpha)$ at all types.

Figure 17 is a CMD for the spectroscopic sample (on-cloud and in-locus) stars with Hα equivalent width measurements. Those stars with $W(\mathrm{H}\alpha) > 10$ Å, i.e., disk candidates, are indicated; of the 205 possible stars 63 (31%) are disk candidates. Table 6 presents the final disk fraction over all ages and masses for this and all the other disk indicators presented later in this section. Although we impose the same in-locus and on-cloud restrictions on all stars represented in these and following figures and Table 6, stars with excesses are more likely to be members than the stars without excesses, so the disk fractions in the table are formally lower limits.

By eye, the disk candidates cover the same region of the CMD as the nondisk candidates. Computing our disk fraction (formally, lower limits to the true disk fraction) as a function of $V-I$, I, age, or mass confirms that, to first order, the disk fraction is constant. There is weak evidence that the disk fraction increases on average toward fainter I or lower masses; there is no evidence for an increase in disk fraction in younger stars.

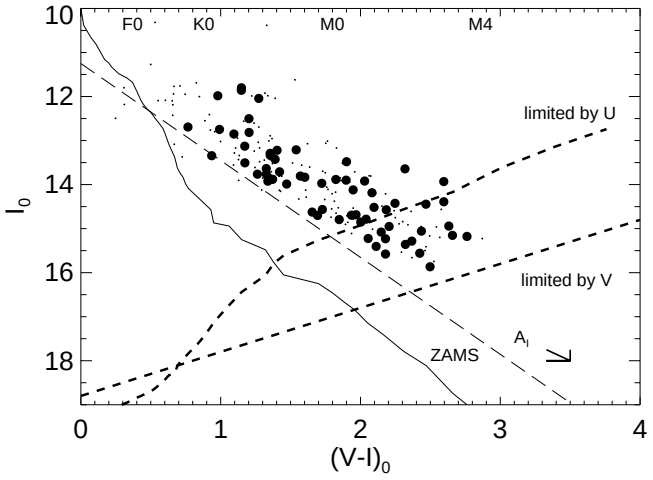

FIG. 17.—CMD with Hα disk candidates indicated (for stars on-cloud and in-locus). Notation is as in Fig. 3, except the larger symbols denote the disk candidates. This is necessarily just the spectroscopic sample, as we have no measurements of Hα for the ensemble. Further, stars only appear here if Hα can be measured from the spectrum. By eye, the disk candidates seem to represent the same fraction of stars throughout the diagram, an impression that is confirmed when the disk fraction is calculated as a function of $V-I$, I, age, or mass.

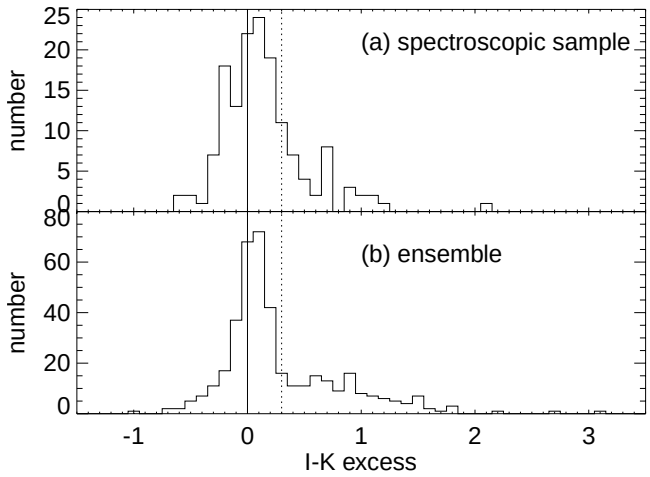

FIG. 18.—Distribution of $I-K$ excesses for the on-cloud and in-locus sample. A vertical solid line has been placed at 0 mag excess to guide the eye, and a dotted vertical line has been placed at 0.3 mag as in Hillenbrand et al. (1998) and R01 to separate the disk candidates (*to the right of the line*) from the nondisk candidates.

TABLE 6
Disk Fractions Derived from Various Indicators

Indicator	Spectroscopic Sample			Ensemble Sample		
	Total Stars[a]	Disks[a]	Mismatches[b]	Total Stars[a]	Disks[a]	Mismatches[b]
Hα	205	63 (31%)	...	...	...	...
$I-K$	150	38 (25%)	...	401	131 (33%)	...
$H-K$	150	33 (22%)	...	401	102 (25%)	...
$U-V$	138	77 (56%)	...	306	167 (55%)	...
$I-K$ and $H-K$	150	27 (18%)	17 (11%)	401	87 (22%)	59 (15%)
$I-K$ and Hα	146	24 (16%)	39 (27%)	...	...	...
$H-K$ and Hα	146	24 (16%)	33 (23%)	...	...	...
$U-V$ and Hα	132	37 (28%)	41 (31%)	...	...	...
$U-V$ and $I-K$	104	24 (23%)	45 (43%)	208	49 (24%)	80 (38%)
$U-V$ and $H-K$	104	20 (19%)	45 (43%)	208	48 (23%)	75 (36%)
$I-K$, $H-K$, and Hα	146	22 (15%)	44 (30%)	...	...	...
$I-K$, $H-K$, and $U-V$	104	18 (17%)	52 (50%)	208	42 (20%)	89 (43%)
$I-K$, $H-K$, $U-V$, Hα	100	16 (16%)	53 (53%)	...	...	...

Notes.—(1) The subsample of stars used to calculate these fractions is the union of the on-cloud and in-locus subsamples (see text). (2) Because we do not have unambiguous membership indicators, strictly speaking, the disk fractions reported here are lower limits to the true disk fraction found in the cluster.

[a] On lines where more than one disk indicator is considered, all disk indicators must exist and must agree on whether or not a star has a disk for the star to be included in these columns.

[b] On lines where more than one disk indicator is considered, this column denotes percentage of entire available sample where there is incomplete agreement, e.g., of the sample with measurements for each indicator, this is the fraction where (at least) one of the disk indicators disagrees with the other disk indicator(s).

6.2. *Near-Infrared Disk Candidates*

Disk candidates may also be identified from near-infrared excesses, thought to be produced from thermal heating and accretion activity in the inner disk. In this study we use two near-IR disk indicators, $I-K$ and $H-K$ excesses (abbreviated here with the shorthand IK excess and HK excess). We refer to R00, R01, and Hillenbrand et al. (1998) for discussions of the definition of these excesses and the relative merits of near-IR disk indicators. Here, we simply remind the reader here that near-IR excesses are more effective than UV excesses at diagnosing the presence of disks for stars with higher $T_{\rm eff}$ but are subject to uncertainties due to inclination and center disk hole effects. As in these earlier papers, excesses are calculated by comparing the dereddened observed color with the expected photospheric color and disk candidates selected as those objects with color excesses greater than 2–3 σ away from the peak. A histogram of IK excesses is shown in Figure 18; as in R01 and

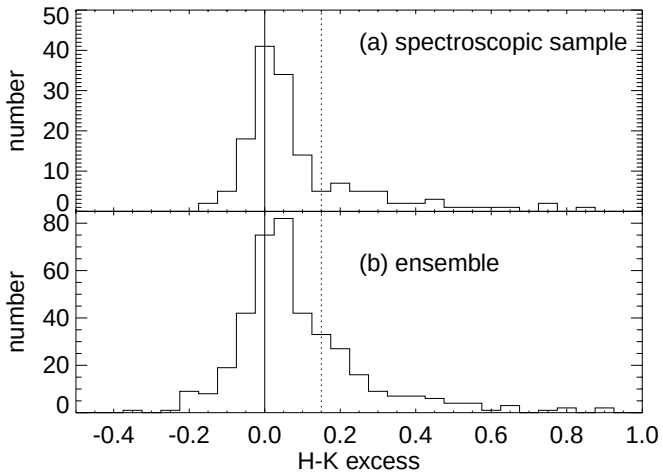

Fig. 19.—Distribution of $H-K$ excesses for the on-cloud and in-locus sample. Disk candidates are stars with an excess >0.15 mag based on a Gaussian fit to this distribution. A vertical solid line has been placed at 0 mag excess to guide the eye, and a dotted vertical line has been placed at 0.15 mag to separate the disk candidates (*to the right of the line*) from the nondisk candidates.

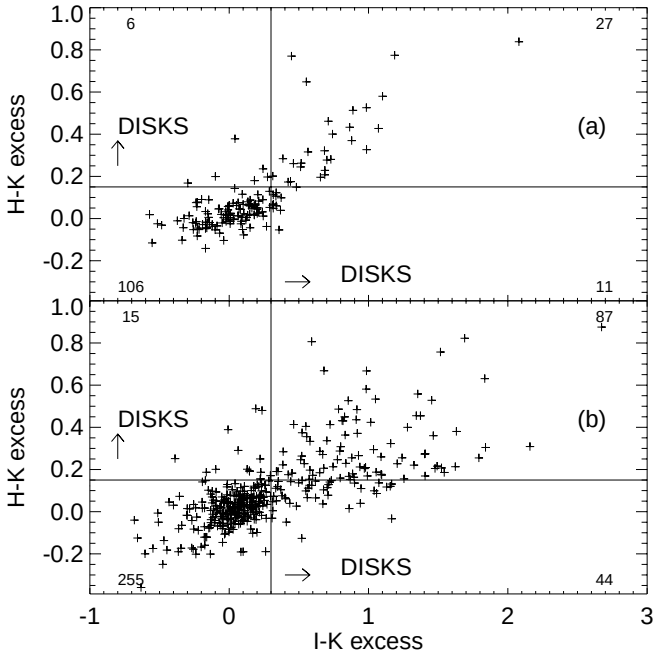

Fig. 20.—$H-K$ excess vs. $I-K$ excess: (*a*) for the spectroscopic (on-cloud, in-locus) sample, and (*b*) for the ensemble (on-cloud, in-locus). Lines marking the disk selection cutoff are indicated. Small numbers in the corners are the number of stars contained in that quadrant and can be used to find, for example, the percentage of stars with $I-K$ excesses that also have $H-K$ excesses. The correlation is quite high; in (*a*) only 11% of the stars have only one positive disk indicator, and in (*b*) 15% of the stars have only one positive disk indicator, most of which are $I-K$ excesses.

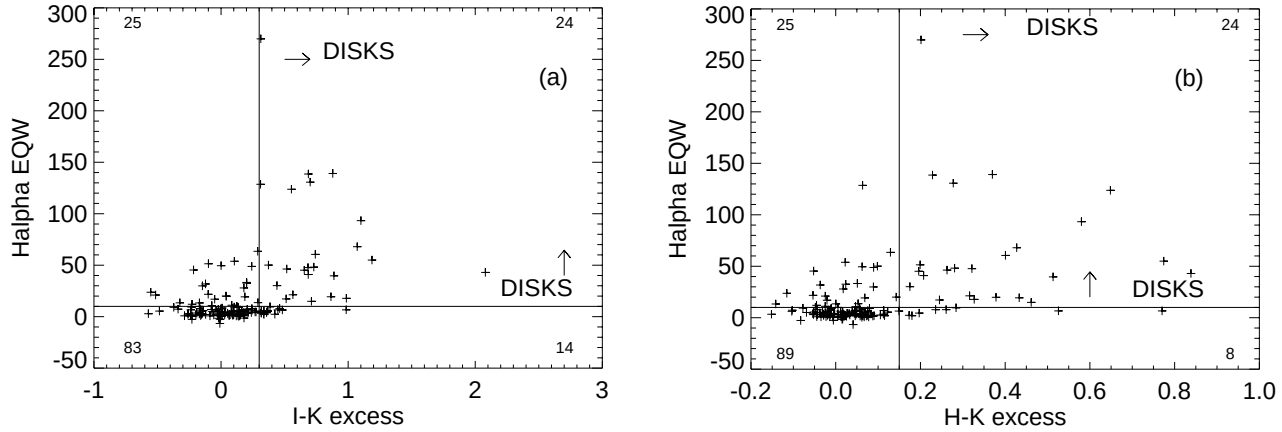

FIG. 21.—Comparison of near-IR disk indicators and Hα EQW, (*a*) $I-K$ excess vs. Hα, and (*b*) $H-K$ excess vs. Hα. Notation is as in Fig. 20. This is necessarily just the spectroscopic subset, as Hα only exists for that sample; as usual, these are just the on-cloud and in-locus stars. Again, note the high degree of correlation; in (*a*) 27% of sample has only one disk indicator, and in (*b*) 23% of sample has only one disk indicator.

Hillenbrand et al. (1998), stars with more than 0.3 mag excess are identified as disk candidates. For the HK excesses, we followed the same procedure as in R01 but reevaluated the cutoff for consideration as a disk candidate based on a Gaussian fit to the distribution in Figure 19*a*. We use 0.15 mag, 2.5 σ away from the peak of the distribution.

Although these two disk indicators are not strictly independent, it is useful to compare them for stars with both indicators measured. Figure 20 compares these excesses for the spectroscopic sample (Fig. 20*a*) and the ensemble of photometry (Fig. 20*b*) for stars both on-cloud and in-locus. Note that in general the correlation is quite good. In both samples, there are more stars with IK excesses but without HK excesses than there are HK excesses with no IK excesses. For a given photometric error, IK is a more sensitive disk indicator than HK, as we found in R01. However, we note that the *JHK* data were acquired simultaneously, while the *I* data were obtained 4 years later. Since these stars are intrinsically variable, IK is potentially more subject to inaccuracies. However, if the random variability of these stars is primarily responsible for the difference in disk detection using the HK and IK indicators, the variability would have to act in such a way to systematically increase the incidence of IK excess, which seems statistically unlikely.

We relate both the HK and IK excess indicators to Hα in Figure 21. Since Hα is thought to arise in accretion columns and near-IR excesses are thought to originate in the disk itself, these disk indicators are then truly independent measures of disk presence. The correlation between them is good but not perfect. Note that the Hα data were taken at different times than any of the photometric data; as such, the intrinsic variability of the stars (both spectroscopic and photometric) may affect the correlation between the indicators. Among the mismatches (where a star is identified as a disk candidate along only one of the two axes in Fig. 21) it is more common for a star to have strong Hα without near-IR excess than to display near-IR excess without strong Hα. It is possible that this is a result of extreme chromospheric activity. It is also possible that there are gas disks around some of these stars, which produce Hα emission without enough dust heating to produce an IR excess. Stars with disks bright in the near-IR but disk accretion rates too small to produce, $W(\mathrm{H}\alpha) > 10$ Å might have appeared here as a substantial population of stars with strong near-IR emission but no Hα emission; note that we do not find such a population.

As above, final aggregate disk fractions for our sample (formally, lower limits to the true disk fractions) can be found in Table 6, along with disk fractions of stars with, for example, both Hα and IK excesses. Similarly, in Figures 22 and 23, we plot a CMD with IK and HK disk candidates indicated, respectively. As in the case of Hα disk candidates above, the disk candidates appear to be smoothly distributed through the sampled region of the CMD. Formal disk fractions calculated for the spectroscopic and ensemble samples and IK excesses suggest that the disk fraction is constant with $V-I$, I, age, and mass. Similar calculations

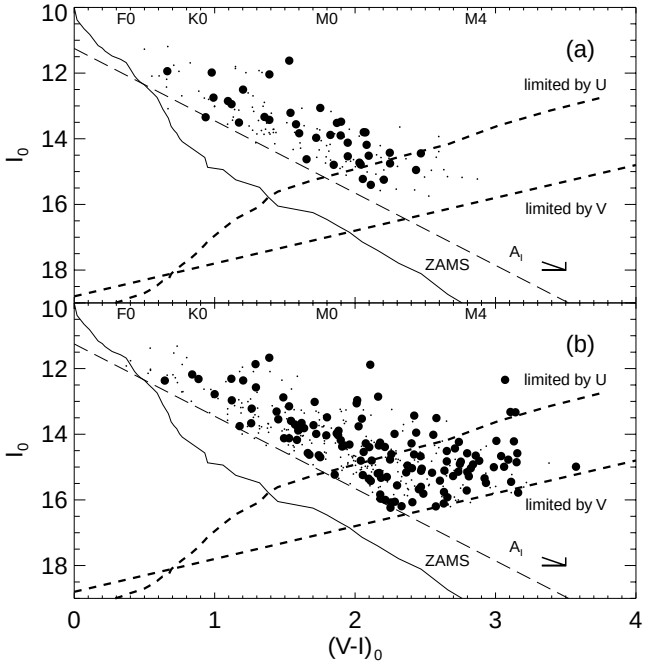

FIG. 22.—CMD for (*a*) spectroscopic sample and (*b*) ensemble with $I-K$ excess disk candidates indicated, limited to on-cloud and in-locus populations. Notation is as in Fig. 17, where the large symbols correspond to disk candidates. As in the case of Hα disk candidates above, the disk candidates here appear to be smoothly distributed through the sampled region of the CMD, an impression that is confirmed by calculating the disk fraction as a function of $V-I$, I, age, and mass.

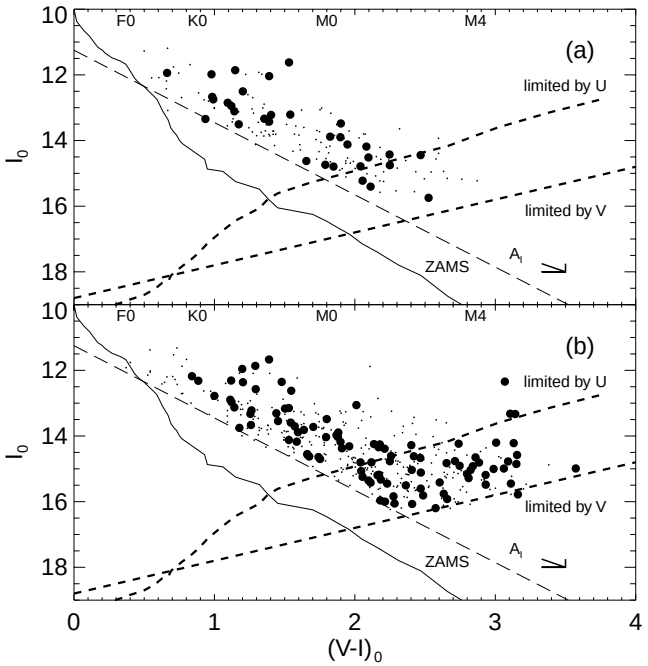

FIG. 23.—CMD for (*a*) spectroscopic sample and (*b*) ensemble with $H-K$ excess disk candidates indicated, limited to on-cloud and in-locus populations. Notation is as in Fig. 17, where the large symbols correspond to disk candidates. As in the case of Hα and $I-K$ disk candidates above, the disk candidates here appear to be smoothly distributed through the sampled region of the CMD, an impression that is confirmed by calculating the disk fraction as a function of $V-I$, I, age, and mass. There is a weak suggestion (at the 1–2 σ level) that the frequency of $H-K$ disks decreases as stars age.

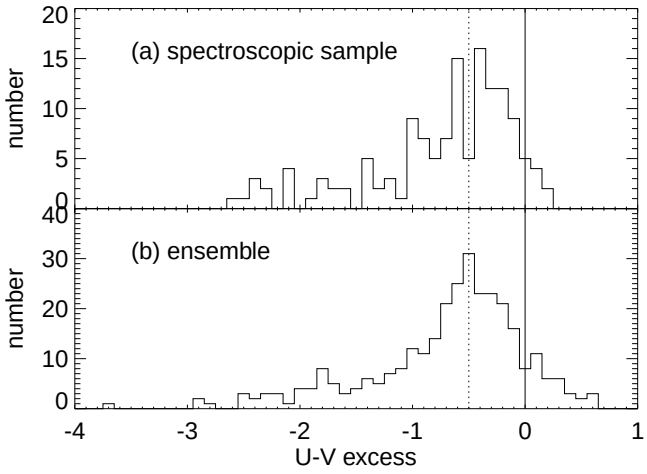

FIG. 24.—Histogram of $U-V$ excesses for the on-cloud and in-locus sample. Disk candidates are stars with an excess bluer than (more negative than) -0.5 mag, as in R00. A vertical solid line has been placed at a 0 mag excess to guide the eye, and a dotted vertical line has been placed at -0.5 mag to separate the disk candidates (*to the left of the line*) from the nondisk candidates.

for the HK excesses suggest (at only the 1–2 σ level) that the frequency of HK disks decreases as stars age (this effect is stronger in the ensemble than in the spectroscopic sample), but is constant as a function of all the other parameters investigated.

6.3. *Ultraviolet Disk Candidates*

Substantial UV emission is thought to arise from shocked material falling in from the disk onto the photosphere. As in R00, we use as a disk indicator the $U-V$ color excess, defined in analogy to $I-K$ and $H-K$ color excess; $U-V$ excess = (dereddened $U-V$)–($U-V$ expected based on spectral type). Note that smaller magnitudes indicate bluer objects, so the more extreme a disk candidate, the more negative the $U-V$ (abbreviated UV) excess. R00 discussed extensively the origin of this excess, the relative merits of this indicator, the effects of using the most likely reddening in its calculation, and the influence of chromospheric activity. We remind the reader that UV excess is a more effective disk indicator than near-IR excesses at later spectral types, because of greater contrast between the shocked emission and the cool photosphere, and that UV excess is more sensitive to reddening corrections, but that insufficient reddening corrections are more likely to drop legitimate candidates than pick up inappropriate candidates. Figure 24 is a histogram of calculated UV excesses for the spectroscopic sample and for the photometric ensemble. We use the same cutoff as in R00, -0.5 mag, as the limit between disk candidates and nondisk candidates. Note that the peak of the UV excess distribution is not zero, suggesting that the majority of stars in each of these samples have some low-level accretion activity.

As in earlier sections, we compare this disk indicator with the other available disk indicators; see Figures 25–27. Since UV excess is expected to probe the same physical processes as Hα, but different processes than those giving rise to the near-IR excesses, we anticipate good correlations with Hα, but not as good correlations with the near-IR excesses (remembering that the UV data, the IR data, and the spectra were obtained at three different times and that intrinsic stellar variability is probably contributing to the scatter). To first order, these expectations are substantiated by the data.

We consider first the comparison with Hα. The basic relationship found between Hα and near-IR excess is that, of the stars with Hα excesses, about half also have near-IR excesses. For the stars with Hα and UV measurements, of the stars with Hα excesses, nearly all of them also have UV excesses. However, of the stars with UV excesses, only

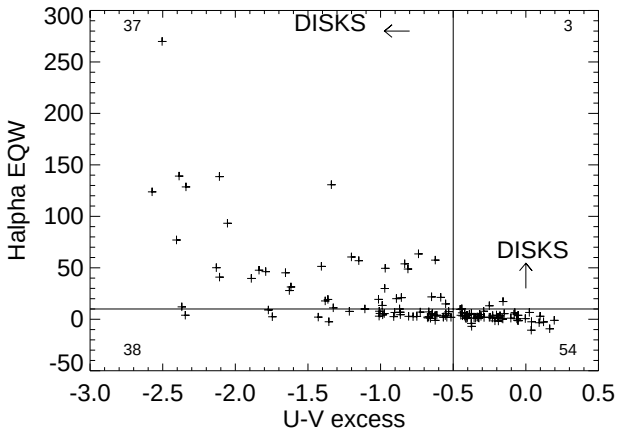

FIG. 25.—$U-V$ excess vs. Hα EQW. Notation is as in earlier figures. This is necessarily just the spectroscopic subset, as Hα only exists for that sample. Again, note high degree of correlation; 31% of sample has only one disk indicator.

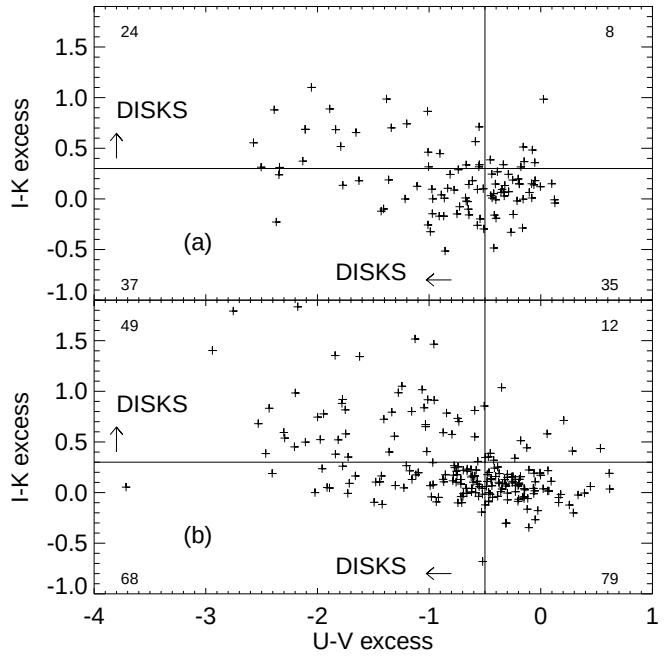

FIG. 26.—$U-V$ excess vs. $I-K$ excess for (*a*) the spectroscopic sample and (*b*) the ensemble (all on-cloud and in-locus). Notation is as in Fig. 20. The correlation between indicators is not as good as it has been in earlier figures like this one; in (*a*) 43% of the sample has only one positive disk indicator, and in (*b*) 38% of the sample has only one positive disk indicator.

about half of them also have Hα excesses. This is basically consistent with our understanding of the origins of these excesses.

Now we compare the UV excesses with the near-IR excesses. A star with an IK or HK excess is often found to have a UV excess as well, but a star with UV excess does not necessarily have either an IK or HK excess. This runs contrary to naive expectations that an accreting star producing a UV excess must obviously have a circumstellar disk and thus should also produce an IR excess. The effect is most dramatic for those stars with substantial UV excesses but undetectable near-IR excesses. We can account for this apparent discrepancy by postulating a large inner disk hole, a pure gaseous disk with a dust optical depth below that needed for an IR excess, or appealing to inclination effects. However, the mass of the star also affects the degree to which we can detect an IR or UV excess. As discussed in more detail in R00 and here in § 7, it is harder to distinguish UV excesses from photospheres in more massive stars, and it is in precisely this realm that near-IR excesses are more easily detected. For less massive stars, the inverse occurs—UV excesses are easily detected, whereas near-IR excesses are harder to detect. In fact, nearly all of the stars with near-IR excesses but no UV excesses are stars more massive than 1 $M_{\odot}$. This mass effect is much less dramatic for our stars with UV excesses but no near-IR excesses; stars ranging in mass from $\sim$0.3–1 $M_{\odot}$ are scattered throughout the left- and bottom-most quadrants of Figure 26. This is most likely a selection effect in that all of the low-mass stars detected in U must also have excesses (low-mass stars without excesses are too faint to be detected in U given our survey limits; see Fig. 12 and Fig. 28). A more complete understanding of the relationship found in Figure 26 awaits detailed modeling of the star-disk system, taking into account disk holes and inclination effects as well as accretion.

Final disk fractions (formal lower limits) can be found in Table 6, along with disk fractions of stars with, for example,

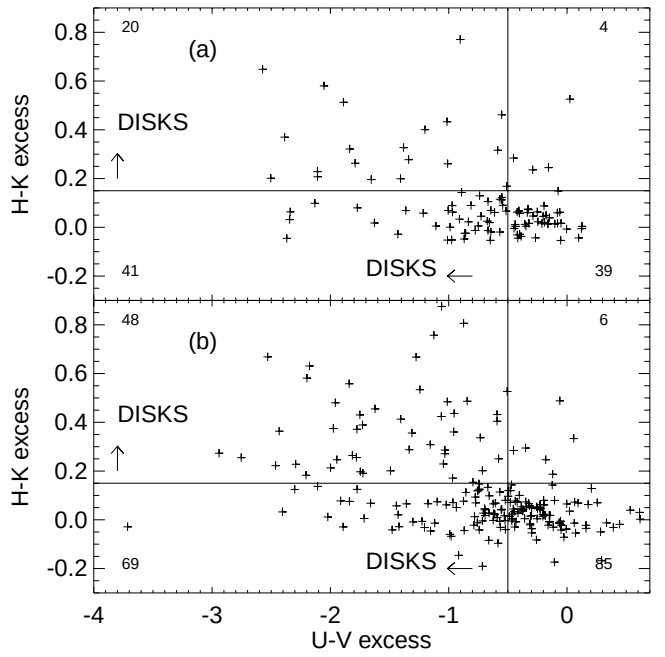

FIG. 27.—$U-V$ excess vs. $H-K$ excess for (*a*) the spectroscopic sample and (*b*) the ensemble (all on-cloud and in-locus). Notation is as in Fig. 20. In (*a*) 43% of the sample has only one positive disk indicator, and in (*b*) 36% of the sample has only one disk indicator.

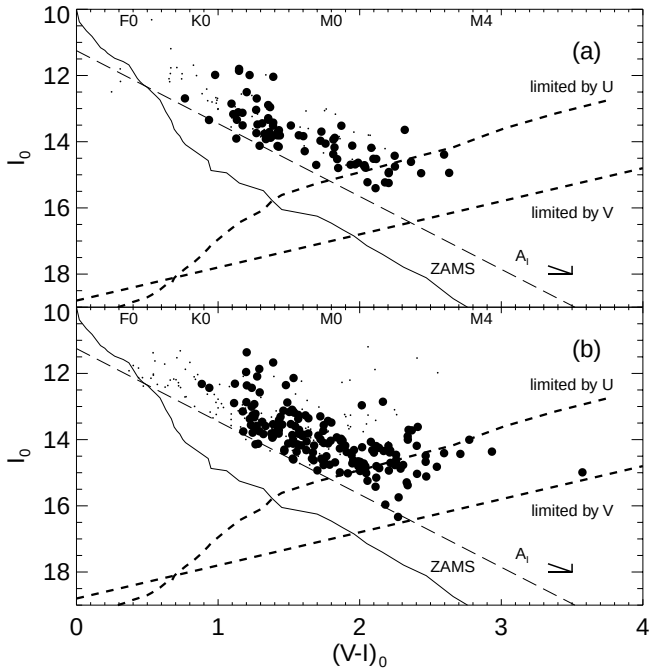

FIG. 28.—CMD for (*a*) the spectroscopic sample and (*b*) the ensemble (both on-cloud and in-locus) with $U-V$ excess disk candidates indicated. Notation is as in Fig. 3. As in the case of the near-IR and Hα disk candidates selected above, the UV disk candidates appear to be smoothly distributed through the sampled region of the CMD, and, as before, formal disk fractions suggest no evidence for a change in disk fraction with $V-I$, I, or mass. There is some evidence that the frequency of UV disks is increasing with age (more strongly in the ensemble than the spectroscopic sample), but this is consistent with our expectations based on the relationship between UV excess, mass accretion rates, and a condensing central mass; see § 7.

both Hα and UV excesses. As in earlier sections, we plot in Figure 28 a CMD with UV disk candidates indicated. As was true in the cases of the near-IR and Hα disk candidates discussed above, the UV disk candidates appear smoothly distributed through the sampled region of the CMD. As before, we calculate formal disk fractions for both the spectroscopic and ensemble photometric samples. Selection effects for these fractions are somewhat more complicated than in earlier sections in that the combination of the U detection limit and the locus position in the CMD means that the faintest stars detected at all in U all have excesses, so the disk fraction rises sharply with the fainter, redder, less massive stars. In the regions of the CMD thought to be less sensitive to this effect, there is no evidence for a change in disk fraction with $V-I$, I, or mass. There is some evidence that the frequency of UV disks is increasing with age (more strongly in the ensemble than the spectroscopic sample), but this is consistent with our expectations based on the relationship between UV excess, mass accretion rates, and a condensing central mass; see § 7 below.

6.4. *Summary of Disk Indicators*

We have identified disk candidates based on Hα, $I-K$, $H-K$, and $U-V$ excesses and have compared the relative efficiencies of these various disk indicators. We found that, in general, the disk indicators track each other quite well. A detailed comparison of the different indicators revealed the different efficiencies of each indicator in different regimes of stellar mass, accretion rate, etc.

Because of a relative lack of membership information for this cluster, the disk fractions we derived are technically lower limits to the true disk fraction of the cluster; we derive disk fractions ranging from 15% to 56%.

Finally, we found an essentially constant distribution of disk candidates and nondisk candidates over the same region of the CMD (stars in-locus and on-cloud, e.g., over the color range $V-I \sim 1$–2.2), regardless of the specific disk indicator used. We detected no statistically significant variation of disk fraction as a function of $V-I$, I, age, or mass for all disk indicators for both the spectroscopic and ensemble samples. There was weak evidence that the frequency of HK disks decreases as stars age and that the frequency of UV disks increases as stars age.

7. MASS ACCRETION RATES

In this section we calculate mass accretion rates $\dot{M}$ for the stars in our data set based on their U-band excesses (§ 7.1) and compare them with those derived by other authors using similar techniques in Taurus-Auriga and Orion (§ 7.2). Following R00, we investigate the implications of our survey sensitivity limits for the detected $\dot{M}$ (§ 7.3) and look for trends in $\dot{M}$ with stellar age and mass (§ 7.4), finding an absence of high $\dot{M}$ values among low-mass stars and among older stars.

7.1. *Calculation of $\dot{M}$*

As in R00, we calculate $\dot{M}$ for our stars based on the excess emission at U, following the methods of Gullbring et al. (1998) and Hartmann et al. (1998). We refer the reader to R00 for a detailed discussion; in summary, based on the dereddened photometry, we calculate the total luminosity emerging in the U band (L_U) convert L_U to an estimate of the accretion luminosity $L_{\rm acc}$ following Gullbring et al., and, finally, derive a value of $\dot{M}$. In the process we make use of an estimate of M_* from DAM models and the R_* derived from the values of $T_{\rm eff}$ and L_* obtained from dereddened photometry.

7.2. *Comparison with Taurus-Auriga and Orion*

Gullbring et al. (1998) derive their relationship between L_U and $L_{\rm acc}$ using stars ranging from K3–M4 in the Taurus-Auriga star-forming region; Hartmann et al. (1998) apply this same formula to derive $\dot{M}$ for stars between K6 and M2.5 in both the Taurus-Auriga and Chameleon star-forming regions. Data taken from the Hartmann et al. analysis of Taurus-Auriga and from R00 for the Orion flanking fields are included in Figures 29–30. The remainder of this figure will be discussed below, but note for now that our range of $V-I$ and $\dot{M}$ overlaps well with the ranges of the other studies, even though NGC 2264, at ~3–5 Myr, is thought to be slightly older than Orion (~1–3 Myr) and slightly younger than Taurus-Auriga (~1–10 Myr). The $\dot{M}$ derived for our targets is typically $\sim 10^{-8}\ M_\odot\ {\rm yr}^{-1}$, with values ranging from $\sim 10^{-9}$–$10^{-6.5}\ M_\odot\ {\rm yr}^{-1}$.

7.3. *Effective Limits in $\dot{M}$*

As we realized in R00, before correlating $\dot{M}$ values with, e.g., stellar mass and age, we need to understand the selection effects inherent to our survey, which limit our ability to find disk candidates at both the hot and cool extremes. From Figures 5 and 11, it is easy to see that the range of UV excesses exhibited increases as $V-I$ increases. We find few disk candidates earlier than ~K5, and essentially all of the stars fainter than our U cutoff are disk candidates. (The U cutoff was propagated into the CMD using ZAMS colors, and so the latest stars bright enough in U to be detected must be significantly brighter in U than the ZAMS counterpart, i.e., they are disk candidates.) In R00 we quantified our sensitivity to disk detection as a function of the stellar

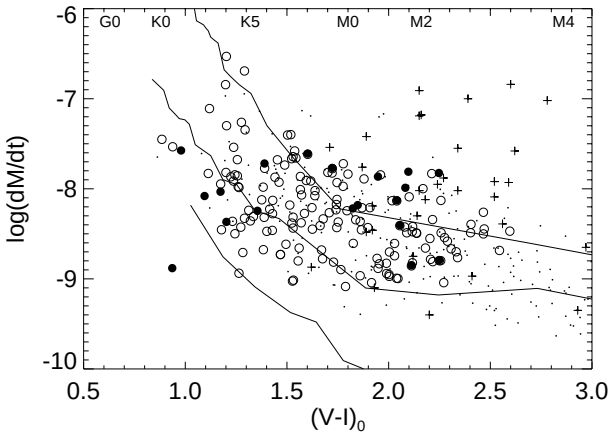

FIG. 29.—$\dot{M}$ vs. $V-I$ for the ensemble (on-cloud and in-locus). Rates derived here are plotted as circles; open circles have UV excesses, solid circles have both UV and IK excesses (note that stars portrayed as open circles in some cases lack $I-K$ measurements or have no IK excess). Data from Hartman et al. (1998) in Taurus-Auriga are crosses, and data from the R00 ensemble in the Orion flanking fields are dots. Lines are simple model calculations of minimum detectable $\dot{M}$ for 0.1, 1, and 10 Myr (*top to bottom*); note overall selection effects (see text). Our range of $V-I$ and $\dot{M}$ overlaps well with the ranges of the other studies, even though NGC 2264, at ~3–5 Myr, is thought to be slightly older than Orion (~1–3 Myr) and slightly younger than Taurus-Auriga (~1–10 Myr).

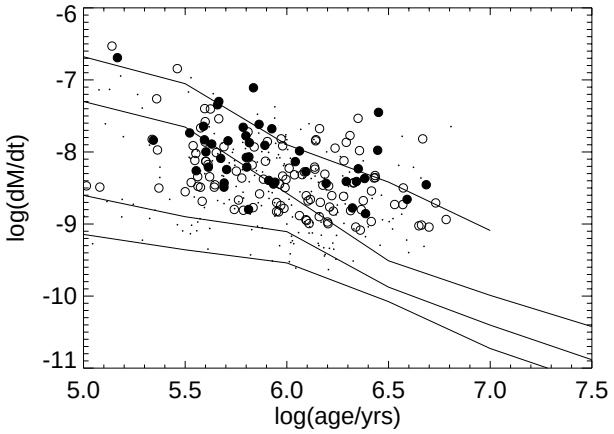

FIG. 30.—$\dot{M}$ vs. age for the ensemble (on-cloud and in-locus). Rates derived here are plotted as circles; open circles have UV excesses, and solid circles have UV and IK excesses (note that stars portrayed as open circles in some cases lack $I-K$ measurements or have no IK excess). Data from the ensemble R00 sample in the Orion flanking fields are dots. Lines are simple model calculations of minimum detectable $\dot{M}$ for (*top to bottom*) 0.9, 0.5, 0.2, and 0.1 $M_{\odot}$; note overall selection effects (see text).

and the accretion properties by constructing extremely simple models, combining Buser & Kurucz (1992) models and an 8000 K blackbody of adjustable surface area superposed on the photosphere to simulate the accretion hot spot. Those models are the origin of the lines in Figures 29–33. Recall that these simple models are meant to demonstrate only the general trends of how the minimum detectable $\dot{M}$ changes in a complex fashion as a function of many variables.

Looking first at the overall trends in the solid lines in Figures 29–31, for types earlier than G–K, the stellar photosphere is sufficiently hot that the addition of an 8000 K spot does not make much detectable difference in the calculated U magnitude; for even earlier types the addition of a spot is not detectable within the simulation to the limits of numerical noise. Moving to cooler stars, the contrast between the stellar photosphere and the accretion hot spot increases, and the spot becomes increasingly easier to detect.

Figures 30–31 are additional views of these simple $\dot{M}$ models, with our data overplotted as a function of mass and age, respectively. As above, the selection effects are complicated. In the next section we investigate the trends present in our data, keeping in mind these approximate trends in detection limits.

7.4. $\dot{M}$ *Trends with Stellar Age and Mass*

To investigate trends of $\dot{M}$ with stellar age and mass, we must be careful to isolate the variable of interest from any of the systematic trends of $\dot{M}$ detectability just outlined. Although we are sensitive to the same ranges of $\dot{M}$ as Hartmann et al. (1998) and R00 (see Fig. 29), we considered in R00 the fact that Hartmann et al. in particular used IR alone to select their disk candidates, and thus their sample may be subtly different from our UV-selected sample, despite the correlation of UV excesses and near-IR excesses demonstrated in Figure 26. Certainly the role of detection limits is different in our case here and in R00, because the UV itself is used as a disk indicator. However, unlike in R00, we have some IR information on these stars as well, and it can be seen in Figures 29–31 that stars with IK as well as UV excesses are generally found scattered through the same region of the diagram occupied by stars with UV excesses.

Figure 32 and 33 show $\dot{M}$ versus age for subsets of the data. The limits in age and mass for $\dot{M}$ measurement as established earlier in the age and mass histograms (Figs. 14*a* and 14*b* and Figs. 15*a* and 15*b*) are also used here. We have shown above that the spectroscopic sample is representative of the photometric sample within the Orion locus, and here it is most useful to interpret trends using the plots with considerably more stars.

These data appear to show systematic trends, but, certainly at the lower envelope, this is driven by the detection

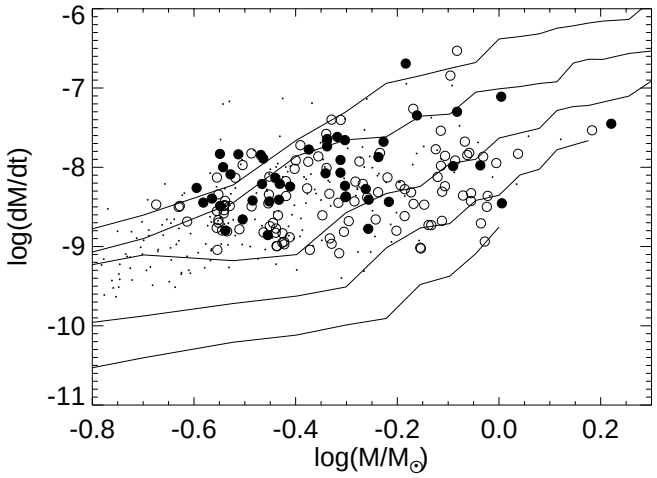

FIG. 31.—$\dot{M}$ vs. mass for the ensemble (on-cloud and in-locus). Rates derived here are plotted as circles; open circles have UV excesses, and solid circles have UV and IK excesses (note that stars portrayed as open circles in some cases lack $I-K$ measurements or have no IK excess). Data from the ensemble R00 sample in the Orion flanking fields are dots. Lines are simple model calculations of minimum detectable $\dot{M}$ for (*top to bottom*) 0.1, 0.3, 1, 3, and 10 Myr; note overall selection effects (see text).

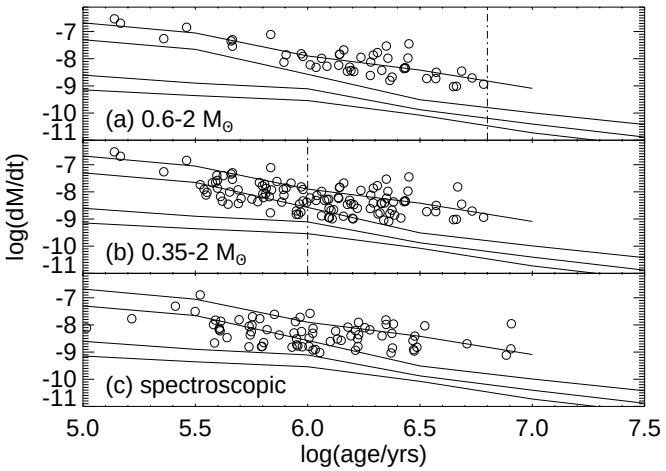

FIG. 32.—$\dot{M}$ vs. age for (*a*) the ensemble limited to 0.6–2 $M_{\odot}$, (*b*) the ensemble limited to 0.35–2 $M_{\odot}$, and (*c*) the spectroscopic sample (all on-cloud and in-locus). Vertical dashed lines denote approximate completeness limits, as in Fig. 14; data are most complete to the left of the line. Solid lines are simple model calculations of minimum detectable $\dot{M}$ for (*top to bottom*) 0.1, 0.3, 1, 3, and 10 Myr (see text). These data appear to show systematic trends, but certainly at the lower envelope this is driven by the detection limits. The upper envelope, however, suggests a lack of low-mass stars with high $\dot{M}$, even though such stars could be readily detected.

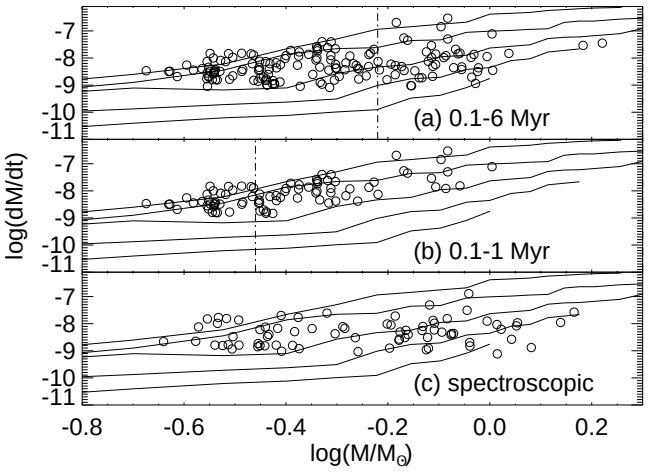

FIG. 33.—$\dot{M}$ vs. mass for (*a*) the ensemble limited to 0.1–6 Myr, (*b*) the ensemble limited to 0.1–1 Myr, and (*c*) the spectroscopic sample (all on-cloud and in-locus). Vertical dashed lines denote approximate completeness limits, as in Fig. 15; data are most complete to the right of the line. Solid lines are simple model calculations of minimum detectable $\dot{M}$ for (*top to bottom*) 0.9, 0.5, 0.2, and 0.1 $M_\odot$ (see text). The lack of stars with high accretion rates and low masses is real, and identical to that found in Orion. However, given the shallower detection limits in NGC 2264, we cannot make as strong a statement about the limits as we did in Orion.

limits. The upper envelope, however, suggests a lack of low-mass stars with high $\dot{M}$, even though such stars could be readily detected.

Recall that the significantly larger population of stars (at similar masses and ages) without a UV excess or for which we could not measure a *U* magnitude necessarily constitutes a population of stars with accretion rates that are much less than those seen in these figures. The interaction of all of the selection effects and sensitivity issues results in the brightest candidates (those with highest $\dot{M}$) being more readily detected in each age bin and an overall trend that resembles the detection limits. However, Figure 14 reveals explicitly how many stars were observed to contribute to the final selection of disk candidates. For example, in Figure 14*c* $\sim$230 stars are observed (most with *U* below our threshold) between ages $10^{6.1}$ and $10^{6.5}$ yr to produce the $\sim$45 stars with *U* excesses in that range. Although we should be sensitive to stars with $\dot{M} \sim 10^{-7}\ M_\odot\ \mathrm{yr}^{-1}$ at ages $\sim 10^{6.3}$ yr in Figure 32*a*, we do not see them, even though we detect stars with these accretion rates at younger ages. This hole is still present in Figure 32*b*, but the completeness limit prevents us from drawing any firm conclusions. In Figure 32*c*, the spectroscopic sample, there is still a lack of older stars with higher $\dot{M}$. Although any trends found in this data may be masked by selection effects, this lack of older stars with higher accretion rates is real, and identical to that found in Orion.

Similarly, in Figure 33 the lower envelope of the data tracks the detection limits, and the upper envelope of the data is not as sensitive to the detection limits. We are still detecting only the brightest stars in each range of masses. But note that we should be sensitive to stars near $\log(M/M_\odot) \sim -0.4$ with accretion rates $\sim 10^{-7}\ M_\odot\ \mathrm{yr}^{-1}$, and we do not see them. For stars with $-0.45 < \log(M/M_\odot) < -0.35$, of the 72 stars observed in *VI* (most with *U* below our threshold), 25 stars have a UV excess, and none of them have $\dot{M} > 10^{-7.5}\ M_\odot\ \mathrm{yr}^{-1}$. The lack of stars with high accretion rates and low masses is real, and identical to that found in Orion. However, given the shallower detection limits in NGC 2264, we cannot make as strong a statement about the limits as we did in Orion.

In conclusion, although we should be sensitive to stars with ages 1–3 Myr and high $\dot{M}$, we do not see them; nor do we see stars with low masses and high $\dot{M}$. Although the selection effects are complicated, we believe the lack of stars in these ranges is real and indicates the presence of real characteristics of the change of $\dot{M}$ with stellar age and mass.

8. CONCLUSIONS

In this optical and near-infrared study of NGC 2264 we have come to the following major conclusions:

1. We have identified disk candidates using $U-V$ excess, $I-K$ excess, $H-K$ excess, and Hα equivalent width. In general, we found good correlation between disk indicators in that most of the stars found to be disk candidates (or not disk candidates) in one method are also disk candidates (or not disk candidates) in another method.
2. As a result of the limited membership information available, the disk fractions we derived are technically lower limits to the true disk fraction; we derived values ranging from 21% to 56%.
3. We found essentially identical distributions of disk candidates and nondisk candidates over the same region of the CMD, regardless of the specific disk indicator used. We found no statistically significant variation of disk fraction as a function of $V-I$, I, age, or mass for all disk indicators, for both the spectroscopic and ensemble samples.
4. We calculated mass accretion rates ($\dot{M}$) for our stars with *U*-band excesses and compared these values with those derived previously for Orion and Taurus-Auriga. The $\dot{M}$ derived for our targets is typically $\sim 10^{-8}\ M_\odot\ \mathrm{yr}^{-1}$, comparable to those derived for other clusters.
5. Over the ranges of ages and masses sampled here, we found some evolution of $\dot{M}$. We found that $\dot{M}$ decreases with age over the range $\sim$0.1–5 Myr and increases with mass over the range $\sim$0.25–1 $M_\odot$. This is comparable to results found previously in Orion.

We would like to thank the referee, M. Bessell, for helpful comments. We also wish to thank the WIYN queue observers for obtaining the data for our program. L. M. R. and R. B. M. would also like to thank NOAO for enabling trips to Tucson. The Digitized Sky Surveys used in Figure 1 were produced at the Space Telescope Science Institute under grant NAG W-2166. The images of these surveys are based on photographic data obtained using the Oschin Schmidt Telescope on Palomar Mountain and the UK Schmidt Telescope. The plates were processed into the present compressed digital form with the permission of these institutions. This research has made extensive use of NASA's Astrophysics Data System Abstract Service and the Astronomical Data Center at NASA Goddard Space Flight Center. S. E. S. acknowledges support from the NASA Origins of Solar Systems program. The research described in this paper was partially carried out at the Jet Propulsion Laboratory, California Institute of Technology, under a contract with the National Aeronautics and Space Administration.

REFERENCES

Adams, M., Strom, K., & Strom, S. 1983, ApJS, 53, 893
Allen, L. E., & Strom, S. E. 1995, AJ, 109, 1379
Bessell, M. S. 1991, AJ, 101, 662
Buser, R., & Kurucz, R. L. 1992, A&A, 264, 557
Calvet, N., Hartmann, L., & Strom, S. 2000, in Protostars and Planets IV, ed. V. Mannings, A. P. Boss, & S. S. Russell (Tucson: Univ. Arizona Press), 377
D'Antona, F., & Mazzitelli, I. 1994, ApJS, 90, 467 (DAM)
Fitzpatrick, E. L. 1999, PASP, 111, 63
Flaccomio, E., Micela, G., Sciortino, S., Damiani, F., Favata, F., Harnden, R., & Schachter, J. 2000, A&A, 355, 651
Flaccomio, E., Micela, G., Sciortino, S., Favata, F., Corbally, C., & Tomaney, A. 1999, A&A, 345, 521
Genzel, R., Reid, M. J., Moran, J. M., & Downes, D. 1981, ApJ, 244, 884
Gullbring, E., Hartmann, L., Briceno, C., & Calvet, N. 1998, ApJ, 492, 323
Hartmann, L., Calvet, N., Gullbring, E., & D'Alessio, P. 1998, ApJ, 495, 385
Herbig, G. 1954, ApJ, 119, 483
Hillenbrand, L. 1997, AJ, 113, 1733
Hillenbrand, L., Strom, S., Calvet, N., Merrill, K. M., Gatley, I., Makidon, R., Meyer, M., & Skrutskie, M. 1998, AJ, 116, 1816
Hollenbach, D., Yorke, H., & Johnstone, D. 2000, in Protostars and Planets IV, ed. V. Mannings, A. P. Boss & S. S. Russell (Tucson: Univ. Arizona Press), 401
Jones, B. F., & Walker, M. F. 1988, AJ, 99, 1755
Kirkpatrick, J. D., Henry, T. J., & McCarthy, D. W. 1991, ApJS, 77, 417
Lada, C., Young, E., & Greene, T. 1993, ApJ, 408, 471
Landolt, A. U. 1992, AJ, 104, 340
Leggett, S. K. 1992, ApJS, 82, 351
Leggett, S. K., Allard, F., & Hauschildt, P. H. 1998, ApJ, 509, 836
Makidon, R., et al. 2002, in preparation
Mathis, J. S. 1990, ARA&A, 28, 37
Monet, D., et al. 1998, USNO-SA2.0 (Washington: US Nav. Obs.)
Najita, J., Edwards, S., Basri, G., & Carr, J. 2000, in Protostars and Planets IV, ed. V. Mannings, A. P. Boss, & S. S. Russell (Tucson: Univ. Arizona Press), 457
Ogura, K. 1984, PASJ, 36, 139
Park, B., Sung, H., Bessell, M., & Kang, Y. 2000, AJ, 120, 894
Patten, B., Simon, T., Strom, S., & Strom, K. 1994, in 8th Cambridge Workshop on Cool Stars, Stellar Systems, and the Sun, ed. J.-P. Caillault (San Francisco: ASP), 125
Rebull, L. M., 2001, AJ, 121, 1676
Rebull, L. M., Hillenbrand, L. A., Strom, S. E., Duncan, D. K., Patten, B. M., Pavlovsky, C., Makidon, R., & Adams, M. 2000, AJ, 119, 3026 (R00)
Sargent, A., & Beckwith, S. 1994, Ap&SS, 212, 181
Siess, L., Dufour, E., & Forestini, M. 2000, A&A, 358, 593 (SDF)
Simon, T., Cash, W., & Snow, T. P., Jr. 1985, ApJ, 293, 542
Strom, K., et al. 1989, AJ, 97, 1451
———. 1990, ApJ, 362, 168
Strom, K., Strom, S., & Merrill, K. 1993, ApJ, 412, 233
Sung, H., Bessell, M. S., & Lee, S.-W. 1997, AJ, 114, 2644
Walker, M. F. 1969, ApJ, 155, 447
Wolf-Chase, G., Walker, C., & Lada, C. 1995, ApJ, 442, 197